

# Fracture evolution in concrete compressive fatigue experiments based on X-ray micro-CT images

Ł. Skarżyński, I. Marzec and J. Tejchman

Faculty of Civil and Environmental Engineering

Gdańsk University of Technology, Poland

*lskarzyn@pg.edu.pl, irek@pg.edu.pl, tejchmk@pg.edu.pl*

## Abstract

This study examines the fatigue performance of plain concrete specimens under uniaxial compression. The experimental program was developed for investigating the fracture evolution in concrete cubic specimens subjected to cyclic compression using the advanced X-ray micro-computed tomography system SkyScan 1173. As compared to other experiments, the 3D micro-CT damage images were shown for a various number of loading cycles. The quantitative evolution of the cracking volume with increasing damage revealed a strongly non-linear shape. The increase of the total crack volume was higher by 30% as compared to the monotonic fatigue test.

**Keywords:** micro-CT; plain concrete; compression; fatigue; fracture; meso-structure

## 1. Introduction

Fatigue is a process of progressive and permanent structural damage in materials which are subjected to repeatedly applied stresses and strains. As a result, macro-cracks or complete fracture occur after a certain number of repeated loading. The knowledge on the concrete behaviour in fatigue is essential for describing the behaviour of different engineering structures under repeated loads with random and varying amplitudes (e.g. concrete bridge desks, highway pavements, railway slab tracks, crane beams, wind power tower bases). The concrete fatigue is still a challenging topic in research works. In particular, the knowledge on the effect of cyclic loading on the evolution of fracture (crack initiation and growth, crack pattern, crack shape, crack number etc.) is still very limited in spite of many laboratory tests (e.g. [1-10]). This problem is also difficult since fatigue displacements and strains are subjected to a pronounced statistical scatter [11]. The progressive decreasing of the compression strength of concrete under cyclic loads happens due to internal damage. The fatigue test results on concrete in compression (mainly low and medium-cycle results) are usually described with the aid of the so-called Wöhler-curve or S-N curve ([2], [12-16]), that shows a linear relationship between the logarithm of the cycles' number

35 and maximum fraction of the monotonic compressive strength. There exist several factors that affect  
36 concrete fatigue behaviour. The fatigue strength mainly depends on the maximum and minimum stress  
37 in the cycle (often identified as the live load and dead load). An increase of the minimum stress and a  
38 decrease of the maximum stress level result in the increased fatigue strength for a given number of  
39 cycles. The frequency between 1 and 15 Hz has a little effect on the fatigue strength provided that the  
40 maximum stress is lower than about 75% of the monotonic strength. At higher stresses, the fatigue  
41 strength decreases with decreasing frequency ([16, 17]). The fatigue strength is also affected by water-  
42 cement ratio, cement content, amount of entrained air, concrete class, rest periods, curing conditions and  
43 age during loading [13]. It is assumed that damage linearly increases with the number of cycles applied  
44 at a certain stress level [17]. The strain at the concrete failure during fatigue tests corresponds to that at  
45 the peak load during quasi-static tests [18]. The failure meso-mechanism in concrete in fatigue  
46 compressive tests is almost the same as in monotonic compressive tests [19].

47

48 The presented research work is experimentally oriented. It is aimed at quantitative investigations of  
49 a three-dimensional (3D) crack evolution in plain concrete under uniaxial fatigue compression loading  
50 with very advanced non-destructive X-ray micro-computed tomography system SkyScan 1173 [20].  
51 Micro-computed tomography (in short ‘micro-CT’) is a 3D imaging technique that uses X-rays to see  
52 the interior of different materials [21]. The micro-CT device performs 2D planar X-ray images and  
53 reconstructs the data into 2D cross-sectional slices that are further processed to obtain a full 3D image.  
54 Thus the volumetric information about changes in the internal micro/meso-structure may be achieved.  
55 In the paper, attention was focused on changes in the fracture volume with an increasing number of  
56 loading cycles in concrete compressive fatigue experiments. This knowledge is important to better  
57 understand a fracture process for enhancing the fatigue life of concrete members and structures. Our  
58 tomography system SkyScan 1173 was already successfully used for observations of a 3D fracture  
59 process inside concrete during different quasi-static monotonic tests: bending [22], uniaxial compression  
60 [23], tension splitting [24] and wedge splitting [25]. The micro-CT images of the concrete structure  
61 allowed us next for developing a very effective numerical 3D four-phase concrete model (composed of  
62 aggregate, cement matrix, macro-pores and interfacial transitional zones (ITZs)) within the discrete  
63 mechanics [23, 24, 26, 27] and continuum mechanics [22, 28, 29] to realistically reproduce strength,  
64 brittleness and fracture in plain concrete in different tests.

5

6 The novel elements of the current paper on concrete fatigue in compression are: 1) the full 3D damage  
7 maps with high-resolution of fractured concrete specimens for the different number of loading cycles in  
8 fatigue compression by considering concrete meso-structure (aggregate, cement matrix and pores) and  
9 2) the quantitative estimation of changes of the cracks’ and pores’ volume (based on 3D damage maps)



70 with increasing cycle number and damage. Our experimental results may create a solid comparative  
71 basis for numerical calculations using different fatigue continuum models for concrete based on  
72 fracture/damage mechanics (e.g. [30-34]) or discrete mechanics ([35]). The micro-CT studies were also  
73 carried out for steel fiber-reinforced concrete under low cycle fatigue in uniaxial compression by Vicente  
74 et al. [19] that indicated a similar crack pattern in specimens under monotonic and cyclic loads. However,  
75 the 2D images of concrete specimens were shown only and the micro-CT scans were solely made at the  
76 beginning and end of tests. The micro-CT technique was also used in fatigue loading tests for scanning  
77 of other engineering materials ([36, 37]). To our knowledge, 3D micro-CT scans of concrete specimens  
78 at different loading cycles in fatigue compression have not been performed yet.

79

## 80 **2. Specimen preparation, experimental set-up and distribution of pores**

81

### 82 **Specimen preparation**

83 The laboratory fatigue experiments on concrete in uniaxial compression were carried out at the Gdansk  
84 University of Technology. The concrete specimens were composed of an ordinary Portland cement  
85 (CEM I 32.5 R), sand and gravel particles and water. The round-shape sand and gravel particles were  
86 used with the maximum diameter of  $d_{\max}=16$  mm, mean diameter of  $d_{50}=2$  mm and particle volume of  
87  $\beta=75\%$  (Figure 1). The water/cement ratio was fixed to 0.42. The composition of the concrete mix was  
88 described in Table 1. A small super plasticizer quantity was used to improve the workability of the fresh  
89 concrete. The tests were carried out on relatively small concrete cubes of  $40\times 40\times 40$  mm<sup>3</sup> to obtain a  
90 very high resolution of 3D micro-CT images of fractured concrete specimens. The cubes were cut out  
91 from the same concrete block of the size  $500\times 500\times 200$  mm<sup>3</sup> after the seventh day. The concrete block  
92 was covered with a plastic sheet during the initial curing period to avoid the surface evaporation and  
93 autogenous shrinkage. They were next kept for 28 days in water. The uniaxial compressive strength  $f_c$   
94 was measured on three cube concrete specimens  $10\times 10\times 10$  cm<sup>3</sup> and Young's modulus  $E$  and Poisson's  
95 ratio  $\nu$  were determined on three cylindrical concrete specimens  $15\times 30$  cm<sup>2</sup>. The mean measured values  
96 were:  $f_c=51.81$  MPa with the standard deviation of 3.36 MPa,  $E=36.1$  GPa with the standard deviation  
97 of 2.29 GPa and  $\nu=0.22$  with the standard deviation of 0.03. The mean tensile strength during three-point  
98 bending on three concrete specimens  $4\times 4\times 16$  cm<sup>2</sup> was 4.04 MPa. The monotonic and fatigue tests were  
99 conducted using the servo-hydraulic machine Zwick Roell HB250 (Figure 2) with the maximum loading  
0 capacity of 250 kN and maximum frequency of 15 Hz. The machine was equipped with two compressive  
1 steel plates and the cubes were always loaded along the casting direction (vertical axis). A sinusoidal  
2 vertical force was applied along the top boundary in fatigue tests. The vertical force  $F$  and the axial  
3 displacement  $u$  were continuously monitored and recorded. Initially, a monotonic test was carried out  
4 with the controlled vertical displacement rate of 0.002 mm/min. The mean maximum vertical force was



105  $F_{max}=81$  kN that results in the uniaxial compressive strength of  $f_c=51.5$  MPa which was almost equal to  
106 the experimental results for the concrete specimens of  $100\times 100\times 100$  mm<sup>3</sup>. Thus the size effect on the  
107 nominal strength was negligible in the tests. However, the size effect on the concrete brittleness existed,  
108 i.e. the ductility was larger for smaller specimens. Next, three cyclic tests were performed on cubic  
109 concrete specimens during which the fatigue test parameters were as follows: the maximum stress  
110  $\sigma_{max}=38.5$  MPa and minimum stress  $\sigma_{min}=19$  MPa with the stress level  $S_{max} = \sigma_{max}/f_c = 0.75$  and  
111  $S_{min} = \sigma_{min}/f_c = 0.37$ , and stress ratio  $R = \sigma_{min}/\sigma_{max}=0.5$ . The frequency of cyclic loading tests  
112 with the constant amplitude was always  $f=2$  Hz. The assumed value of  $S$  was rational from the point of  
113 the design of concrete members in order to avoid the frequency effect. The frequency variations between  
114 1 and 15 Hz have, namely, an insignificant effect on the fatigue strength provided that the maximum  
115 stress level is smaller than 75% of the monotonic static strength ([16, 17]). The expected fatigue life of  
116 concrete specimens was about  $N=60,000$  cycles according to Model Code 2010 [14] ( $\log N =$   
117  $(12 + 16S_{min} + 8S_{min}^2)(1 - S_{max})$ ). Although the number of concrete specimens was low (3), the  
118 calculated fatigue experimental results were similar with respect to the number of loading cycles leading  
119 specimens to the failure, changes of cracks' and pores' volumes and cracks' distributions.

120

## 121 **Experimental set-up**

122 The cracking evolution in concrete during fatigue cyclic tests was investigated using the advanced  
123 X-ray micro-computed tomography system SkyScan 1173 (Figure 3). This system represents the newest  
124 generation in high-resolution desktop X-ray micro-tomography technologies for 3D scanning [20]. The  
125 technology defines the density of each specimen voxel by assigning different shades of grey (light grey  
126 shades correspond to high densities and dark grey shades correspond to low densities). The system was  
127 equipped with the high energy table open scanner with the 130 keV micro-focus X-ray source, flat panel  
128 sensor of the large format (5 Mpx) and special protection by a lead-glass fiber-optic window (Figure 3).  
129 The scanner possessed a precision object manipulator that allowed for a very precise and automatic  
130 specimen positioning. There were several filters available in the front of the  
131 X-ray detector: 0.25 mm brass filter, 1.0 mm aluminium filter, 2.0 mm lead filter and 0.25 mm copper  
132 filter. As compared to usual micro-tomography systems, it has two important advantages: a) large  
133 specimens up to 200 mm in diameter may be scanned and b) the specimens may be scanned with the  
134 high precision of 2-3 microns. During tests on concrete cubes, the X-ray source voltage was set on  
5 130 keV, current on 61  $\mu$ A and exposure time on 4000 ms. The pixel size was 34.2  $\mu$ m. The X-ray  
6 projections were recorded with the rotation increment of 0.2° within 360°. To reduce the noise in X-ray  
7 projections, the frame averaging option was chosen to be 6 and the random movement option 10. The  
8 scanning time was equal to 6 hours. All specimens were scanned using the same input parameters. In  
9 order to recognize pores and cracks on micro-CT scans, a threshold procedure was carefully performed,



140 based on the density of each concrete phase. The threshold in the range 0-60 from the grey level  
141 histogram 0-255 was chosen. The image reconstruction was carried out with the NRecon software. After  
142 the reconstruction, the images were analyzed with the CTAn software and finally the CTVox software  
143 was used to prepare the volume-rendering image reconstruction. The software programs were developed  
144 by the firm Bruker micro-CT (<https://www.bruker.com/products/microtomography.html>).

145

146 Figure 4 presents the view on three cubic specimens  $40 \times 40 \times 40 \text{ mm}^3$  (called the specimens '1'-'3')  
147 before fatigue tests, based on the 3D micro-CT images. The micro-CT technology clearly reveals a  
148 heterogeneous 3D material meso-structure where aggregate, cement matrix, and pores are  
149 distinguishable on the images of specimens. The porous interfacial transitional zones (ITZs) around  
150 aggregate grains that are a very important concrete phase in inducing micro-cracks and attracting macro-  
151 cracks [26, 27] are not visible in scans due to their very small dimensions. However, they may be  
152 observed and measured on the concrete surface e.g. with the aid of the 2D scanning electron microscope  
153 (SEM) ([22-24]). The width of FPZs may be determined on the concrete surface by means of the digital  
154 image correlation (DIC) technique ([22-24]).

155

### 156 **Distribution of pores**

157 Figure 5 and Table 2 show the initial 3D distribution and content of pores in non-cracked concrete  
158 specimens '1'-'3' (intended for fatigue tests) of Figure 4 and '0' (intended for monotonic test). The pores  
159 were divided into the so-called closed and open ones. The open pores were defined as the pores that  
160 spread beyond the borders of the investigated specimen and the closed pores were defined as those in  
161 the specimen's interior. The initial pore volume in the specimens '1'-'3' was  $1568.4 \text{ mm}^3$ , i.e. 2.45% of  
162 the specimen volume (closed pores - 1.60% and open pores - 0.85%, Figures 4a and 5a),  $1760.2 \text{ mm}^3$ ,  
163 i.e. 2.75% of the specimen volume (closed pores - 2.07% and open pores - 0.68%, Figures 4b and 5b)  
164 and  $1516.8 \text{ mm}^3$ , i.e. 2.37% of the specimen volume (closed pores - 1.98% and open pores - 0.39, Figures  
165 4c and 5c). The pores with the diameter smaller than 1.0 mm constituted about 25-30%, the pores with  
166 the diameter 1.0 mm - 2.0 mm represented about 20-30% and the pores with the diameter larger than 2.0  
167 mm formed about 40-50% of the total pore volume in concrete specimens. The specimen '0' that was  
168 subjected to monotonic static compression had the similar initial pore volume ( $1817.6 \text{ mm}^3$ ) as the  
169 specimens '1'-'3'.

170

## 171 **3. Experimental results of fatigue compressive tests**

172

173 The fatigue cyclic loading tests were carried out on 3 concrete specimens  $40 \times 40 \times 40 \text{ mm}^3$  with the  
174 control of both the stress level and stress ratio. The continuous fatigue tests were performed for the

175 specimens '1' and '2'. For those specimens, the initial (non-cracked specimens) and final (cracked  
176 specimens) micro-CT images were only shot whereas for the specimen '3', some micro-CT scans were  
177 shot during the entire fatigue test. The specimens were always unloaded for scanning (scanning lasted  
178 each time 6 hours). Next, the compression test was continued. The scanning took place after  $N_i=10,000$ ,  
179 30,000, 60,000 and 70,000 cycles, so in total, five 3D micro-CT scanning series were performed  
180 (including initial scans before the tests). Note that unloaded periods for scanning may slightly affect  
181 fracture since some crack recovery (cracks' closure) occurred during those rest periods [38]. The number  
182 of loading cycles leading specimens to the failure (fatigue life cycles) of the specimens '1'-'3' is shown  
183 in Table 3. It was between  $N=71,000$  and 80,000 cycles (i.e. slightly higher than that (60,000) according  
184 to [14]).

185  
186 The stress-displacement diagrams  $\sigma=f(u)$  for the concrete specimens '1'-'3' during the cyclic fatigue  
187 tests as compared to the monotonic static test is shown in Figure 6. Figure 7 presents the zoom on the  
188 experimental vertical displacement  $u$  of the specimen '3' in cyclic uniaxial compression versus the cycle  
189 number  $N_i$  with the marked breaks for scanning. In the monotonic test, the curve  $\sigma=f(u)$  included  
190 obviously the elastic, hardening and softening region (Figure 6).

191  
192 The external 3D micro-CT images of cubic cracked concrete specimens '1'-'3' and '0' are presented in  
193 Figure 8. The specimens '1'-'3' were scanned close to failure (Table 3) for  $N_i=70,000$  and the observed  
194 pattern of pores including cracks is shown in Figure 9. Table 4 includes the volumes of pores and cracks  
195 in concrete specimens '1'-'3' after 70,000 cycles and in the specimen '0' after the monotonic test.

196  
197 After the tests, the specimens were strongly cracked (Figures 8 and 9). The vertical cracks that  
198 propagated through the entire specimen height were predominant. There existed 6, 2 and 4 main vertical  
199 macro-cracks in the entire concrete specimens '1'-'3' (Figure 8). Moreover, in the specimens '1' and '3'  
200 some diagonal cracks can also be observed. The cracking slightly varied along the height of specimens  
201 due to the effect of boundary conditions in tests [39, 40]. The cracks were curved due to the presence of  
202 stochastically located aggregate particles. Initially, the cracking process was induced due to some stress  
203 concentrations close to the cube corners (see Figures 12 and 13) where the inclined micro-cracks  
204 appeared and coalesced. Next, some vertical cracks started to concentrate along lateral both edges and  
5 surfaces of specimens by forming column-like regions. The macro-cracks were the widest on external  
6 parts of concrete cubes at lateral edges that finally lead to concrete spalling from specimen cores [23],  
7 [41]. The concentration extent of cracking regions throughout the specimen was similar in monotonic  
8 and fatigue tests, based on the visual inspection (compare Figures 9b and 9d). However, wider macro-

209 cracks (compare Figures 9a and 9c) and more damaged aggregate particles were noticed during fatigue  
210 tests.

211

212 Due to cracking, the insignificant volumetric changes of open and the pronounced changes of closed  
213 pores happened during fatigue tests (Table 4, Figure 10). The crack volume was calculated as the total  
214 volume of pores in the cracked specimen reduced by the total volume of pores in the initial non-cracked  
215 specimen. The cracks' volume and the %-volume of open pores increased in all specimens. In contrast,  
216 the %-volume of closed pores decreased in the specimens. The cracks' volume increased during fatigue  
217 test by 3.43%-5.62% in the specimens '1'-'3'. The %-volume of open pores increased by 1.86%-4.38%  
218 and the %-volume of closed pores decreased by 0.2%-0.74%. The increase of the cracks' volume and  
219 open pores in the specimen '0' (monotonic test) was smaller on average by about 30% than during  
220 fatigue tests. The greatest macro-crack width in the entire specimens' volume (after unloading) was  
221  $w_c=0.42$  mm (specimen '0'),  $w_c=0.61$  mm (specimen '1'),  $w_c=0.56$  mm (specimen '2') and  $w_c=0.72$  mm  
222 (specimen '3'). The pores were practically not crossed by cracks since insignificant volume changes of  
223 closed pores took place (connected with strong volume changes of open pores) (Table 4).

224

225 Figure 11 shows the cross-sectional micro-CT images of the cracked specimens '1'-'3' and '0' (one  
226 horizontal and two vertical in the mid-specimen that intersected the specimen centroid). They show that  
227 cracks mainly propagated through the cement matrix and ITZs which were the weakest zones in concrete.  
228 The micro-cracks occurred first in porous ITZs around aggregate particles and then they connected  
229 themselves through a bridging mechanism ([22-24]). When two interfacial cracks happened around  
230 adjacent aggregate particles, a crack inside the cement matrix bridged those interfacial cracks so that a  
231 connected crack path was formed. The cracks also propagated sometimes through single weak aggregate  
232 particles (Figure 12). The cracks' branching also occurred (Figure 12).

233

234 Figures 13 and 14 show the external 3D micro-CT images of the concrete specimen '3' for the different  
235 cycle number  $N_i$ :  $N_1=0$  (step "0" - initial scan),  $N_3=30,000$  (step "2"),  $N_4=60,000$  (step "3") and  
236  $N_5=70,000$  (step "4"). The results for  $N_2=10,000$  were not presented since the cracks insignificantly  
237 developed. The different three cross-sectional micro-CT images of the mid-region (one horizontal and  
238 two vertical that intersected the specimen centroid) for the different number of loading cycles  $N_i$  are  
9 demonstrated in Figure 15.

0

1 For  $N_i=10,000$  cycles (Figure 15B), the thin cracks occurred with the width up to  $w_c=0.04$  mm. The  
2 cracks had an irregular shape and were mainly concentrated along one vertical (lateral) edge of the  
3 specimen. All micro-cracks occurred in ITZs between the cement matrix and aggregate particles and

244 propagated next in the cement matrix. For  $N_3=30,000$  cycles (Figures 13b, 14b and 15C) further  
245 development of existing internal cracks took place (they propagated into the depth of the cement matrix)  
246 and the new macro-cracks occurred (one at the other lateral edge and one on the lateral surface). In total,  
247 7 broken aggregate particles were detected in the entire specimen. The greatest crack width in the entire  
248 volume was  $w_c=0.16$  mm. After  $N_4=60,000$  cycles (Figures 13c, 14c and 15D) the existing vertical  
249 macro-cracks further evolved along lateral edges and two of those cracks propagated through the  
250 specimen height. The maximum crack width was  $w_c=0.42$  mm. The number of broken aggregate particles  
251 was 13. For  $N_5=70,000$  cycles (Figures 13d, 14d and 15E), four main vertical macro-cracks of an  
252 irregular shape and a variable width might be observed (two cracks were located along two lateral edges  
253 and two cracks were concentrated on the lateral surface of the specimen). The macro-cracks intersected  
254 the concrete specimen. In addition, one macro-crack occurred along a horizontal edge and one inclined  
255 macro-crack appeared in the upper region on the second lateral surface. The main macro-cracks were  
256 connected through a network of small cracks. The largest crack width was equal to  $w_c=0.72$  mm. The  
257 number of broken aggregate particles increased up to 28. Finally, the specimen damage occurred along  
258 the edge wherein the dominant vertical macro-crack was located.

259

260 Table 5 and Figures 16 and 17 present the detailed data on the volume changes of pores and cracks in  
261 the concrete specimen '3' with increasing damage parameter (expressed by the quotient of the number  
262 of cycles  $N_i$  and the fatigue life  $N=73,127$ , Table 3). The line connecting the measurement points was  
263 approximated in Figures 16 and 17 by a polynomial function. The volume of closed pores slightly  
264 decreased during the entire test (Figure 16). In the step "1", the insignificant volume changes of open  
265 pores and cracks were obtained as compared to the step '0'. The maximum crack width in the entire  
266 volume was  $w_c=0.04$  mm (after the specimen unloading). In the step "2", the volume of pores and cracks  
267 increased by about 50%. The greatest crack width in the entire volume was  $w_c=0.16$  mm (after the  
268 specimen unloading). In the step "3", the volume of pores and cracks increased as compared to the step  
269 '2' by about 40%. The maximum crack width in the entire volume was  $w_c=0.42$  mm (after the specimen  
270 unloading). In the last step "4", the volume of pores and cracks increased as compared to the step '3' by  
271 about 40%. The largest crack width in the entire volume was  $w_c=0.72$  mm. (after the specimen  
272 unloading). The increase of the cracks' volume with increasing damage parameter was strongly non-  
273 linear. The relationship in Figure 17 may be divided into three parts: 1) between the damage parameter  
4 0 ( $N_1=0$ ) and damage parameter 0.14 ( $N_2=10,000$ ) (so-called the micro-crack part), 2) between the  
5 damage parameter 0.14 ( $N_2=10,000$ ) and damage parameter 0.85 ( $N_4=60,000$ ) (so-called the transitory  
6 part) and 3) between the damage parameter 0.85 ( $N_4=60,000$ ) and damage parameter  $\sim 1.0$  ( $N_5=70,000$ )  
7 (so-called the crack extension part [41]) (Figure 17). The damage rate was in particular strong in the last  
8 fatigue stage (crack extension region) between  $N_4=60,000$  and  $N_5=70,000$  cycles.



279

280 In Figures 18 and 19, the attention is focused on the largest crack volume growth in the crack extension  
281 region before the specimen failure. The volume of cracks between those 2 different cycles' numbers  
282 increased by 2.26% (40% of the total cracks' growth) (Figure 18d, Table 5). The %-volume of closed  
283 pores decreased from 1.34% down to 1.24% (the decrease of about 10%) and the %-volume of open  
284 pores increased from 4.39% up to 6.75% (the increase of about 50%). The width of cracks, which was  
285 very non-uniformly distributed in the specimen, increased on average by 0.1-0.2 mm (Figure 18).  
286 However, in some specimen regions, it increased even by 0.3 mm.

287

288 Our experiments on concrete fatigue will be continued. An extended X-ray micro-computed tomography  
289 system will be used soon, i.e. the tomography system SkyScan 1173 will be connected to the loading  
290 machine ISTRON 5569 to make images of deforming concrete specimens during a continuous  
291 deformation process, i.e. without unloading for scanning.

292

## 293 **4. Conclusions**

294

295 This paper presents the results of experimental research work showing the 3D fracture evolution in plain  
296 concrete specimens under fatigue compression obtained by X-ray micro-CT that is a powerful tool to  
297 measure the internal damage of concrete specimens. For plain concrete under fatigue compression, the  
298 following conclusions can be offered:

299

300 - The increase of the cracks' volume with increasing damage (expressed by the quotient of the number  
301 of cycles and fatigue life) was about hyperbolic in shape. The volume of cracks close to the failure  
302 load was 3.4-5.6% of the entire specimen volume during fatigue tests. Due to cracking, the %-volume  
303 of closed pores decreased by about 30% and the %-volume of open pores increased 5-15 times. In the  
304 last loading stage between 60,000 and 70,000 cycles, the cracks' volume strongly increased (by 2.26%),  
305 i.e. almost 40% of the total crack volumetric growth.

306

307 - The growth of the total fracture volume in fatigue tests was higher by 30% as compared to the  
308 monotonic test.

9

0 - A similar crack pattern was obtained in specimens under monotonic and cyclic loading although the  
1 latter was on more damaged. The cracking pattern was strongly non-uniform. The greatest cracks' width  
2 was in the range of 0.56-0.72 mm (fatigue tests) and 0.42 mm (monotonic test). The cracks that initially  
3 occurred in ITZs and propagated through the cement matrix by bridging, were strongly curved. However,

314 several cracks also propagated through weak aggregate particles. At the failure, the lateral sides of  
315 specimens separated from the cores.

316

### 317 **Acknowledgements**

318 Research work has been carried out as a part of the Project: “*Innovative resources and effective methods*  
319 *of safety improvement and durability of buildings and transport infrastructure in the sustainable*  
320 *development*” financed by the European Union (POIG.01.01.02-10- 106/09-01) and of the Project “*Effect*  
321 *of concrete meso-structure on initiation and propagation of cracks - experiments and two-scale*  
322 *numerical model*” financed by the National Science Centre (NCN) (UMO-2017/25/B/ST8/02108).

323

### 324 **References**

- 325 [1] Aas-Jakobsen K. Fatigue of concrete beams and columns. *Institute for Betonkonstruktioner Bulletin*  
326 1970; 70(1).
- 327 [2] Tepfers R, Kutti T. Fatigue strength of plain and ordinary and lightweight concrete. *ACI Journal*,  
328 1979; 76(5): 635-652.
- 329 [3] Hsu TCT. Fatigue of plain concrete. *Journal of the American Concrete Institute* 1981;78(8): 292-  
330 305.
- 331 [4] Petkovic G, Lenschow R, Stemland H, Rosseland S. Fatigue of high-strength concrete, *ACI SP-121:*  
332 *High-strength concrete* 1990 505-525.
- 333 [5] Kim, JL, Kim YY. Experimental study of the fatigue behavior of high strength concrete, *Cement and*  
334 *Concrete Research* 1996;26(10):1513-1523.
- 335 [6] Tue NV, Mucha S. Fatigue behaviour of high strength concrete under compression, *Bautechnik*  
336 2006;83(7):497-504 (in German).
- 337 [7] Lohaus L, Wefer M, Oneschkow N, Design model for the fatigue behaviour of normal strength, high  
338 strength and ultra-high strength concrete. *Beton- und Stahlbetonbau* 2011; 106(12):836–846. (in  
339 German).
- 340 [8] Jiang C, Gu X, Huang Q. Zhang W. Deformation of concrete under high-cycle fatigue loads in  
341 uniaxial and eccentric compression. *Construction and Building Materials* 2017;141:379-39.
- 342 [9] Lu J, Zhu K, Tian L, Guo L. Dynamic compressive strength of concrete damaged by fatigue loading  
343 and freeze-thaw cycling, *Construction and Building Materials* 2017; 15:847-855.
- 4 [10] Fan J, Jiang D, Chen J, Liu W, Ngaha WT, Chen J. Fatigue performance of ordinary concrete under  
5 discontinuous cyclic loading. *Construction and Building Materials* 2018; 166:974-981.
- 6 [11] Liang J, Ding Z, Li J. A probabilistic analyzed method for concrete fatigue life, *Probabilistic*  
7 *Engineering Mechanics* 2017;49:13-21.



- 348 [12] Shi XP, Fwa TF, Tan SA. Flexural fatigue strength of plain concrete, *ACI Materials Journal*  
349 1993;90(5):435-440.
- 350 [13] Lantsoght E, van der Veen C, de Boer A, Proposal for the fatigue strength of concrete under cycles  
351 of compression. *Construction and Building Materials* 2016;107:138-156.
- 352 [14] Model Code 2010. Final draft. FIB Bulletin, EPFL Lausanne 2012.
- 353 [15] Eurocode 2 Design of concrete structures. European Committee for Standardization. EN 1992-  
354 2:2005/AC:2008. Brussels (Belgium): European Standards 2008.
- 355 [16] ACI 215R-74 Considerations for design of concrete structures subjected to fatigue loading. *ACI*  
356 *Committee 215*, 1997; 71(3), 97-121.
- 357 [17] Ceb Committee GTG 15. Fatigue of concrete structures. CEB Bulletin d'information, No 188,  
358 Lausanne, Switzerland: European Concrete Committee, 1988.
- 359 [18] Balázs GL, Fatigue of bond, *ACI Materials Journal* 1991; 88(6):620-629.
- 360 [19] Vicente MA, Ruiz G, Gonzalez DC, Minguez J, Tarifa JM, Zhang XX. CT-Scan study of crack  
361 patterns of fiber-reinforced concrete loaded monotonically and under low-cycle fatigue, *International*  
362 *Journal of Fatigue* 2018; 114:138-147.
- 363 [20] Skarżyński L, Tejchman J. Experimental investigations of fracture process in concrete by means of  
364 X-ray micro-computed tomography. *Strain* 2016;52:26-45.
- 365 [21] Vicente MA, Mínguez J, González DC, Book chapter: the use of computed tomography explore the  
366 microstructure of materials in civil engineering: from rocks to concrete (in: Halefoglou A.M., editor)  
367 *Computed tomography - advanced applications*. InTech, 2017, pp. 207-230.)
- 368 [22] Skarżyński L, Nitka M, Tejchman J. Modelling of concrete fracture at aggregate level using FEM  
369 and DEM based on X-ray  $\mu$ CT images of internal structure. *Engineering Fracture Mechanics* 2015;  
370 147:13-35.
- 371 [23] Suchorzewski J, Tejchman J, Nitka M. DEM simulations of fracture in concrete under uniaxial  
372 compression based on its real internal structure. *Int. J. Damage Mechanics* 2018;27(4):578-607.
- 373 [24] Suchorzewski J, Tejchman J, Nitka M, Experimental and numerical investigations of concrete  
374 behaviour at meso-level during quasi-static splitting tension. *Theoretical and Applied Fracture*  
375 *Mechanics* 2018;96:720-739.
- 376 [25] Skarżyński L, Suchorzewski J. Mechanical and fracture properties of concrete reinforced with  
377 recycled and industrial steel fibers using Digital Image Correlation technique and X-ray micro-computed  
8 tomography. *Construction and Building Materials* 2018;183:283-299.
- 9 [26] Nitka M., Tejchman J. A three-dimensional meso-scale approach to concrete fracture based on  
0 combined DEM with X-ray  $\mu$ CT images. *Cement and Concrete Research* 2018;107:11-29.
- 1 [27] Suchorzewski J, Tejchman J, Nitka M, Bobiński J. Meso-scale analyses of size effect in brittle  
2 materials using DEM. *Granular Matter* 2018 (in review).

- 383 [28] Trawinski, W., Bobinski, J. and Tejchman, J. Two-dimensional simulations of concrete fracture at  
384 aggregate level with cohesive elements based on X-ray micro-CT images. *Engineering Fracture*  
385 *Mechanics* 2016; 168: 201-226.
- 386 [29] Trawiński W, Tejchman J, Bobiński J. A three-dimensional meso-scale approach with cohesive  
387 elements to concrete fracture based on X-ray  $\mu$ CT images. *Engineering Fracture Mechanics* 2018;189:  
388 27-50.
- 389 [30] Ray S, Kishen JMC. Fatigue crack propagation model for plain concrete—An analogy with  
390 population growth, *Engineering Fracture Mechanics* 2010;77:3418–3433.
- 391 [31] Simon KM, Kishen, J.M.C. A multiscale approach for modeling fatigue crack growth in concrete.  
392 *International Journal of Fatigue* 2017;98 :1-13.
- 393 [32] Chaboche JL, Lesne PM. A nonlinear continuous fatigue damage model. *Fatigue & Fracture*  
394 *Engineering Materials & Structures* 1998 ;11:1-17.
- 395 [33] Papa, E, Taliercio A. Anisotropic damage model for the multiaxial static and fatigue behaviour of  
396 plain concrete. *Engineering Fracture Mechanics* 1996;55:163-179.
- 397 [34] Alliche, A. Damage model for fatigue loading of concrete. *International Journal of Fatigue*  
398 2004;26:915-921
- 399 [35] Nguyen NHT, Buia HH, Kodikara J, Aroorana S, Darve F. A discrete element modelling approach  
400 for fatigue damage growth in cemented materials. *International Journal of Plasticity* 2018,  
401 <https://doi.org/10.1016/j.ijplas.2018.08.007>.
- 402 [36] Wagner P, Schwarzhaupt O, May M. In-situ X-ray computed tomography of composites subjected  
403 to fatigue loading. *Materials Letters* 2019;236:128-130.
- 404 [37] Harimon, MA, Miyashita Y, Yuichi Otsuka Y, Mutoh Y, Yamamoto, S. High temperature fatigue  
405 characteristics of P/M and hot-forged W-Re and TZM for X-ray target of CT scanner. *Materials &*  
406 *Design* 218;137:335-344.
- 407 [38] Hilsdorf, HK, Kesler CE. Fatigue Strength of Concrete Under Varying Flexural Stresses. *Proc.*  
408 *American Concrete Institute* 1966; 63:1059-1075.
- 409 [39] van Vliet, MRA, van Mier JGM. Experimental investigation of concrete fracture under uniaxial  
410 compression. *Mechanics of Cohesive-Frictional Materials* 1996;1:115–127.
- 411 [40] del Viso, JR, Carmona, JR, Ruiz G. Shape and size effects on the compressive strength of high-  
412 strength concrete, *Cement and Concrete Research* 2008;38:386-395.
- 3 [41] Li Q, Huang H, Xu S, Zhou B, Yu RC. Compressive fatigue damage and failure mechanism of fiber  
4 reinforced cementitious material with high ductility. *Cement and Concrete Research* 2016;90:174-183.
- 5  
6  
7

## LIST OF FIGURES

418

419

420 **Figure 1:** Particle size distribution curve of concrete (maximum diameter  $d_{max}=16$  mm and mean  
421 diameter  $d_{50}=2$  mm)

422

423 **Figure 2:** Testing servo-hydraulic machine Zwick Roell HB250 with the concrete specimen for fatigue  
424 tests (marked with the arrow)

425

426 **Figure 3:** X-ray micro-tomography station SkyScan 1173 [20]: a) X-ray source, b) flat panel and  
427 c) precision object manipulator

428

429 **Figure 4:** Initial 3D external X-ray micro-CT images of cubic concrete specimens before fatigue tests:  
430 a) specimen '1', b) specimen '2' and c) specimen '3' (black colour denotes pores)

431

432 **Figure 5:** Initial diameter distribution of pores inside of non-cracked concrete specimens of Figure 4  
433 before fatigue tests: a) specimen '1', b) specimen '2' and c) specimen '3' (colours denote diameter in  
434 range of  $\leq 1.0$  mm (red colour), 1.01 mm - 2.0 mm (green colour) and  $\geq 2.0$  mm (blue colour))

435

436 **Figure 6:** Experimental vertical normal stress  $\sigma$  versus vertical displacement  $u$  from monotonic and  
437 cyclic uniaxial compression tests (a) quasi-static test, b) fatigue test '1', c) fatigue test '2' and  
438 d) fatigue test '3')

439

440 **Figure 7:** Experimental vertical displacement  $u$  from cyclic uniaxial compression tests versus the  
441 number of cycles  $N$  for concrete specimen '3' (vertical dashed lines denote breaks for X-ray micro-CT  
442 scanning)

443

444 **Figure 8:** External 3D X-ray micro-CT images of cracked cubic concrete specimens close to failure  
445 during cyclic and monotonic tests in compression: a) specimen '1', b) specimen '2', c) specimen '3' in  
446 cyclic tests and d) specimen '0' in monotonic test (black colour denotes both pores and cracks)

7

8 **Figure 9:** Internal 3D micro-CT images of pores and cracks in cubic concrete specimens close to failure  
9 during cyclic and monotonic tests: a) specimen '1' b) specimen '2', c) specimen '3' in cyclic tests and d)  
0 specimen '0' in monotonic test (colours denote macro-pores' diameter in range of  $\leq 1.0$  mm (red colour),  
1 1.01 mm - 2.0 mm (green colour) and  $\geq 2.0$  mm (blue colour))

452

453 **Figure 10:** Volume changes of pores and cracks in concrete specimens '0'-'3' during uniaxial fatigue  
454 compression: a) volume of closed pores, b) volume of open pores and c) volume of cracks ( $\times$  - initial  
455 value before test and  $\bullet$  - final value after test)

456

457 **Figure 11:** 2D micro-CT images of cracked cubic specimens close to failure: A) specimen '1',  
458 B) specimen '2', C) specimen '3' (fatigue tests) and D) specimen '0' (monotonic test) (a) and b) two  
459 vertical mid-specimen cross-sections and c) horizontal mid-specimen cross-section, black colour denotes  
460 pores and cracks)

461

462 **Figure 12:** View on crack branching and crack propagating through weak aggregate particle

463

464 **Figure 13:** Cracking evolution in cubic concrete specimen '3' from 3D micro-CT images in fatigue tests:  
465 a) before test (Figure 4c), b) after  $N_3=30,000$  cycles c) after  $N_4=60,000$  cycles and d) after  $N_5=70,000$   
466 cycles

467

468 **Figure 14:** Evolution of pores and cracks in cubic concrete specimen '3' from 3D micro-CT images in  
469 fatigue tests: a) before test (Figure 5c), b) after 30,000 loading cycles c) after 60,000 loading cycles and  
470 d) after 70,000 loading cycles colours denote pores' diameter in range of  $\leq 1.0$  mm (red colour), 1.01  
471 mm - 2.0 mm (green colour) and  $\geq 2.0$  mm (blue colour)

472

473 **Figure 15:** 2D micro-CT images of cracked cubic specimen '3' for different deformation steps:  
474 A) step "0", B) step "1", C) step "2", D) step "3" and E) step "4" (a) and b) two vertical mid-specimen  
475 cross-sections and c) horizontal mid-specimen cross-section, black colour denotes pores and macro-  
476 cracks)

477

478 **Figure 16:** Evolution of volume of closed pores (a) and open pores (b) with increasing damage  
479 (expressed by quotient of number of loading cycles  $N_i$  and fatigue life  $N$ ) in concrete specimen '3'

480

481 **Figure 17:** Evolution of crack volume  $V$  versus damage (expressed by quotient of number of loading  
2 cycles  $N_i$  and fatigue life  $N$ ) in concrete specimen '3'

3

4 **Figure 18:** Distribution of pores and cracks in specimen '3': a) non-cracked concrete specimen (white  
5 colour), b) after  $N_4=60,000$  cycles (green colour), c) after  $N_5=70,000$  loading cycles (green and red  
6 colour) and d) between  $N_4=60,000$  and  $N_5=70,000$  cycles (red colour)

487 **Figure 19:** Micro-CT image of distribution of crack width's growth between  $N_4=60,000$  and  $N_5=70,000$   
488 cycles in concrete specimen '3' of Figure 18d

489  
490  
491  
492  
493  
494  
495  
496  
497  
498  
499  
500  
501  
502  
503  
504  
505  
506  
507  
508  
509  
510  
511  
512  
513  
514  
515  
516  
517  
518  
519  
520  
521  
522  
523  
524  
525  
526  
527  
528  
529  
0  
1  
2  
3  
4  
5  
6

MOST WIEDZY Downloaded from mostwiedzy.pl



# LIST OF FIGURES

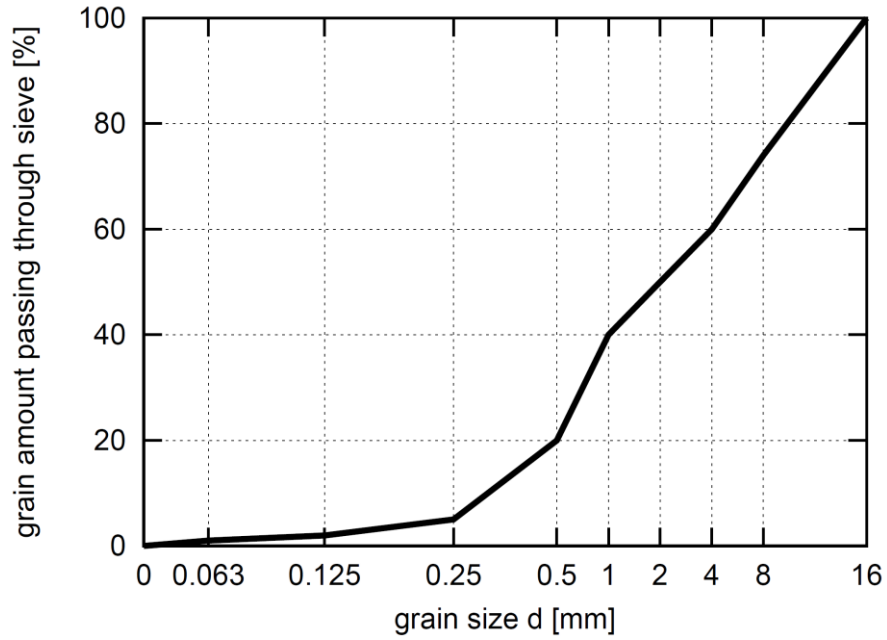
537

538

539

540

541



542

543

544

545

546 **Figure 1:** Particle size distribution curve of concrete (maximum diameter  $d_{max}=16$  mm and mean  
547 diameter  $d_{50}=2$  mm)

548

549

550

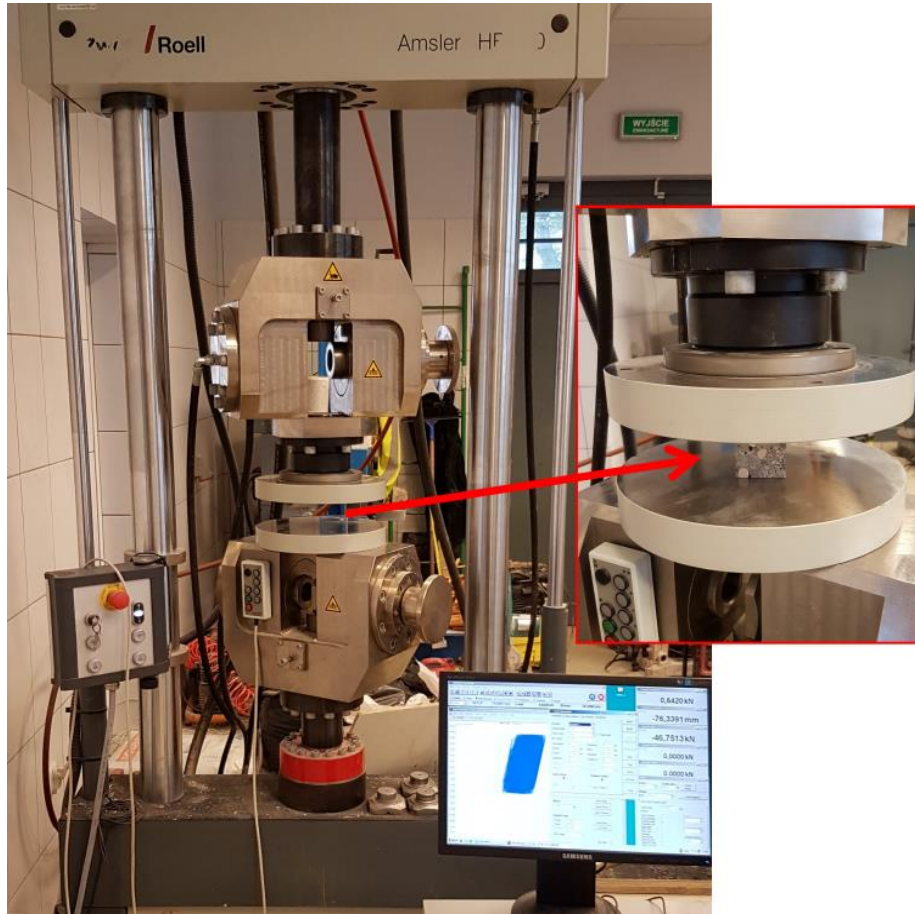
551

552

**FIGURE 1**



553  
554  
555



556

557

558 **Figure 2:** Testing servo-hydraulic machine Zwick Roell HB250 with concrete specimen for the fatigue  
559 tests (marked with the arrow)

560

561

562

563

564

565

## FIGURE 2

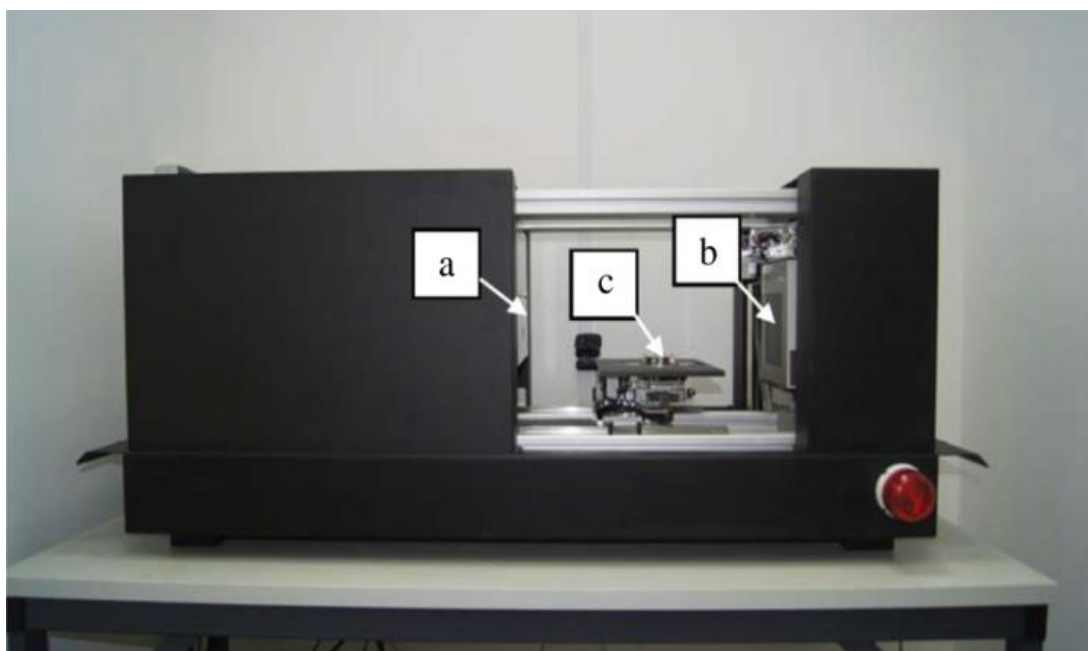
6

7

568

569

570



571

572 **Figure 3:** X-ray micro-tomography station SkyScan 1173 [20]: a) X-ray source, b) flat panel and  
573 c) precision object manipulator

574

575

576

577

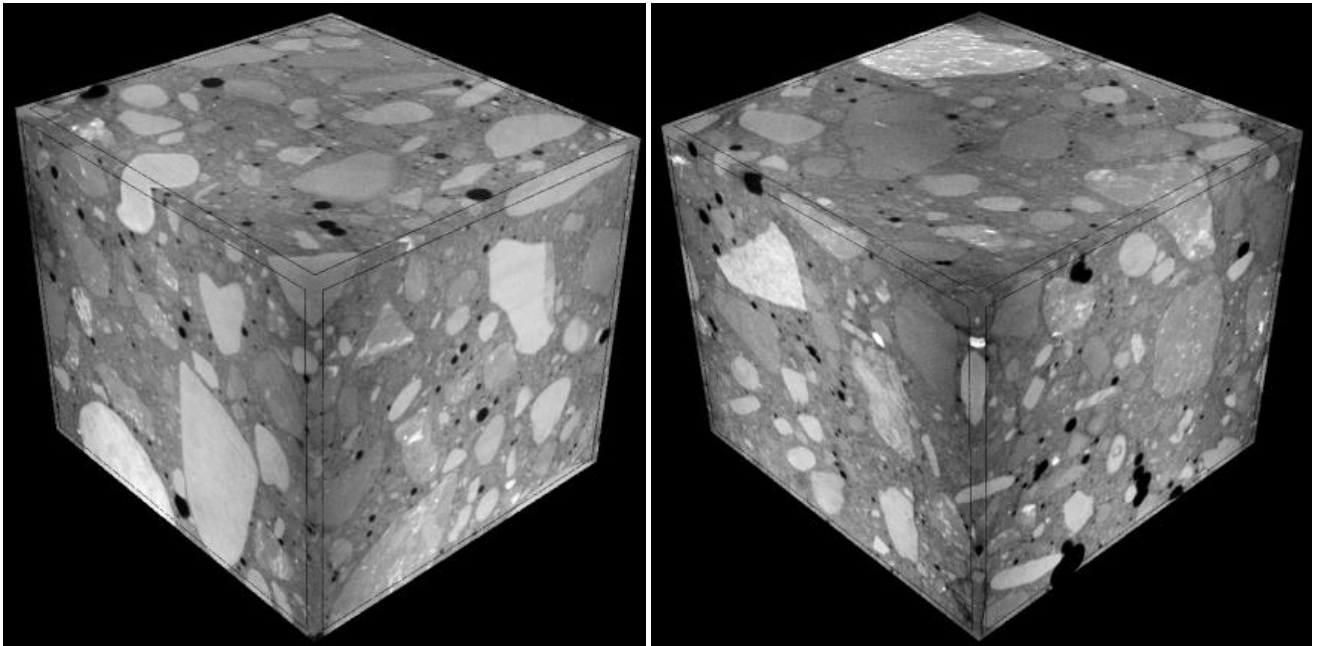
### FIGURE 3

578

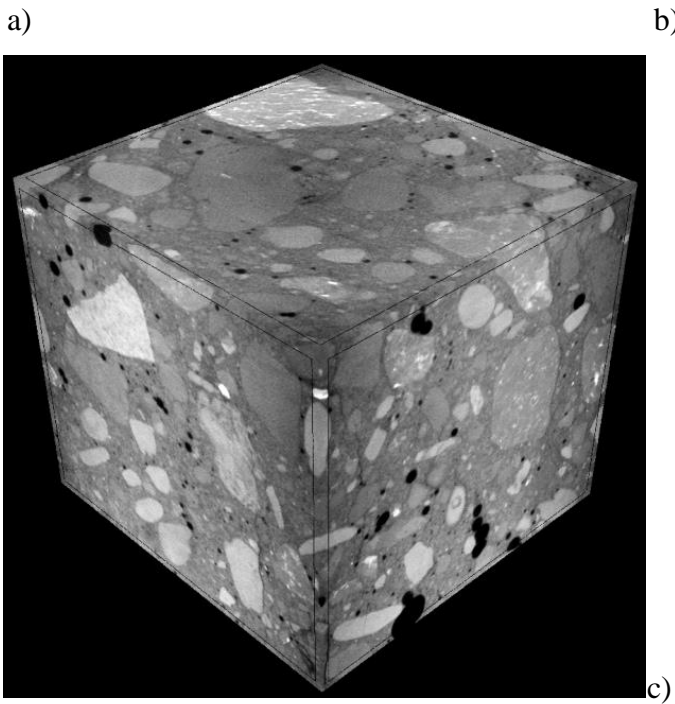
579

580

581  
582  
583



584  
585

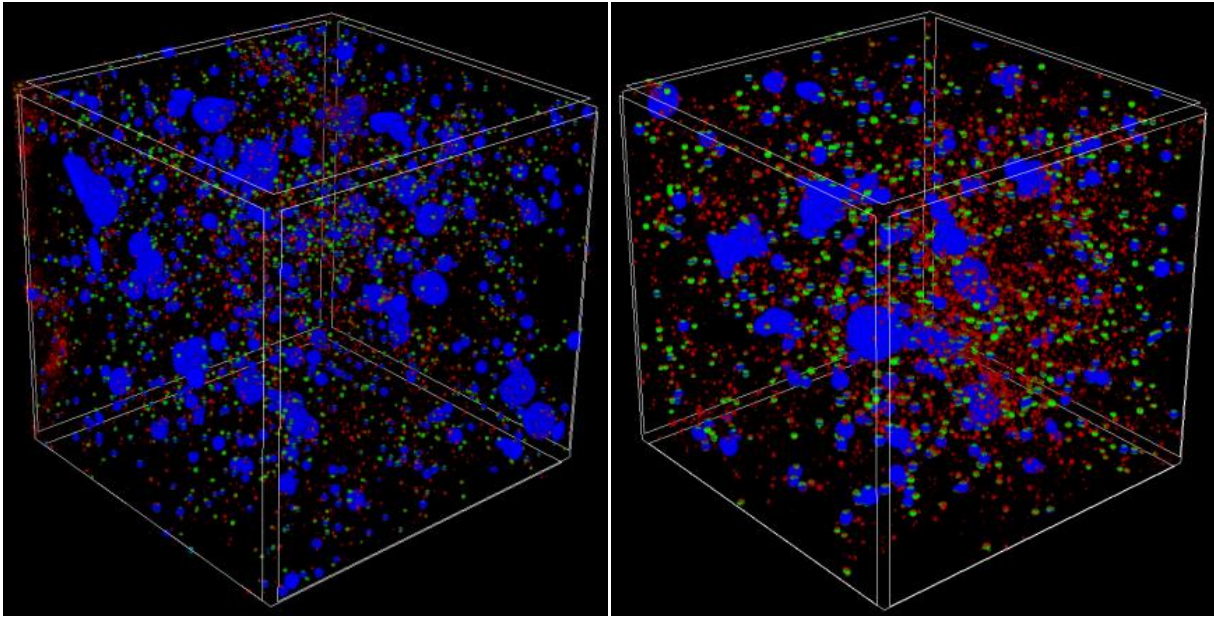


586  
587

588 **Figure 4:** Initial 3D external X-ray micro-CT images of cubic concrete specimens before fatigue tests:  
9 a) specimen '1', b) specimen '2' and c) specimen '3' (black colour denotes pores)

## FIGURE 4

2

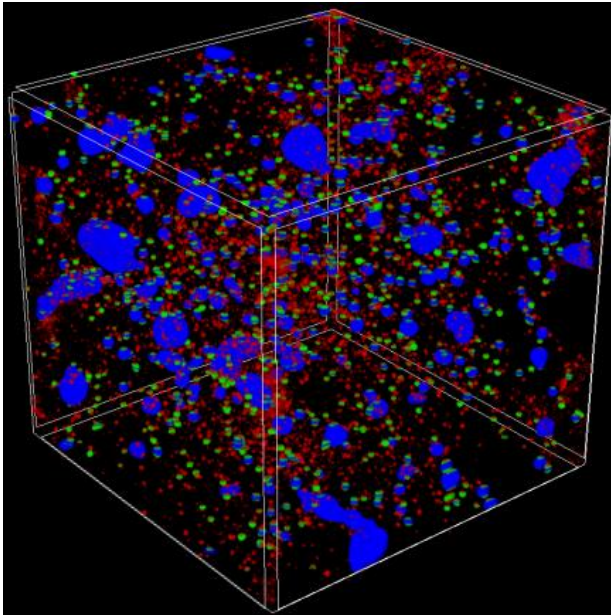


594

595

a)

b)



596

597

598

599

600

601

c)

**Figure 5:** Initial diameter distribution of pores inside of non-cracked concrete specimens of Figure 4 before fatigue tests: a) specimen '1', b) specimen '2' and c) specimen '3' (colours denote diameter in range of  $\leq 1.0$  mm (red colour), 1.01 mm - 2.0 mm (green colour) and  $\geq 2.0$  mm (blue colour))

## FIGURE 5

2

3

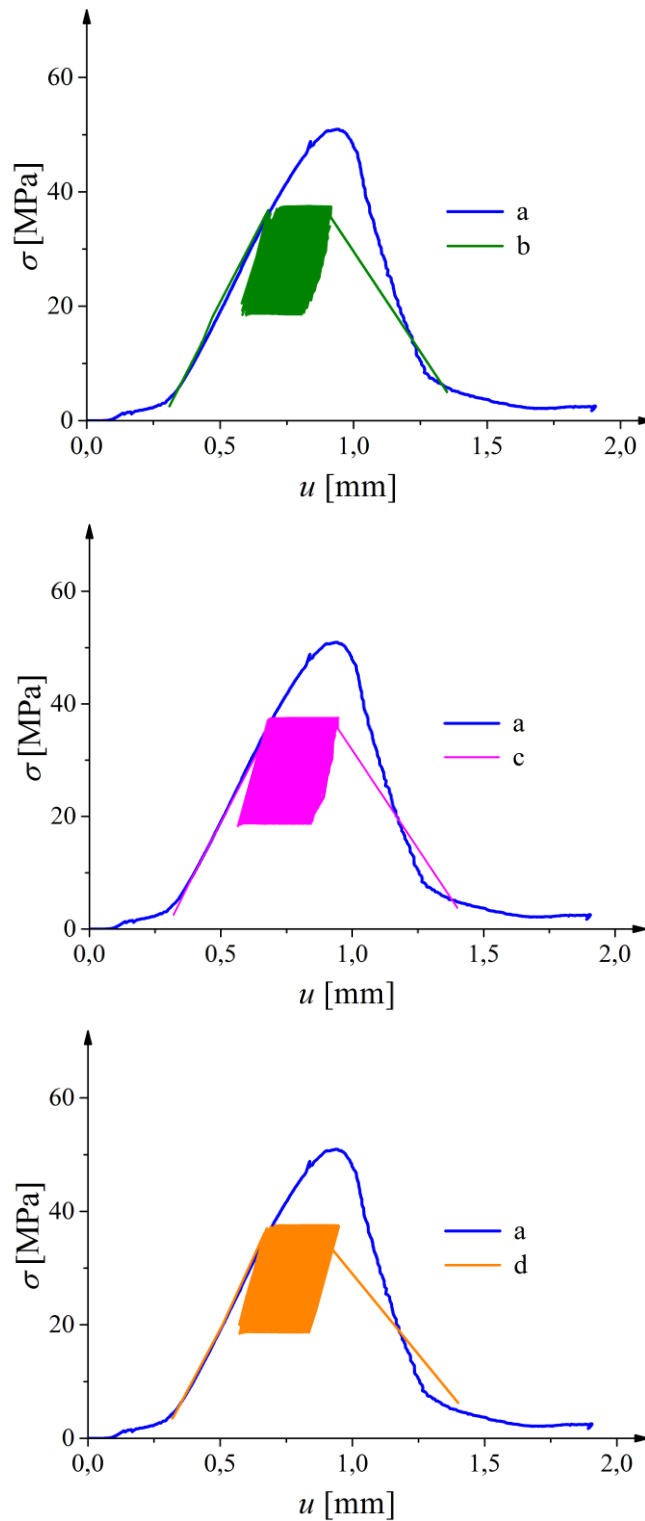
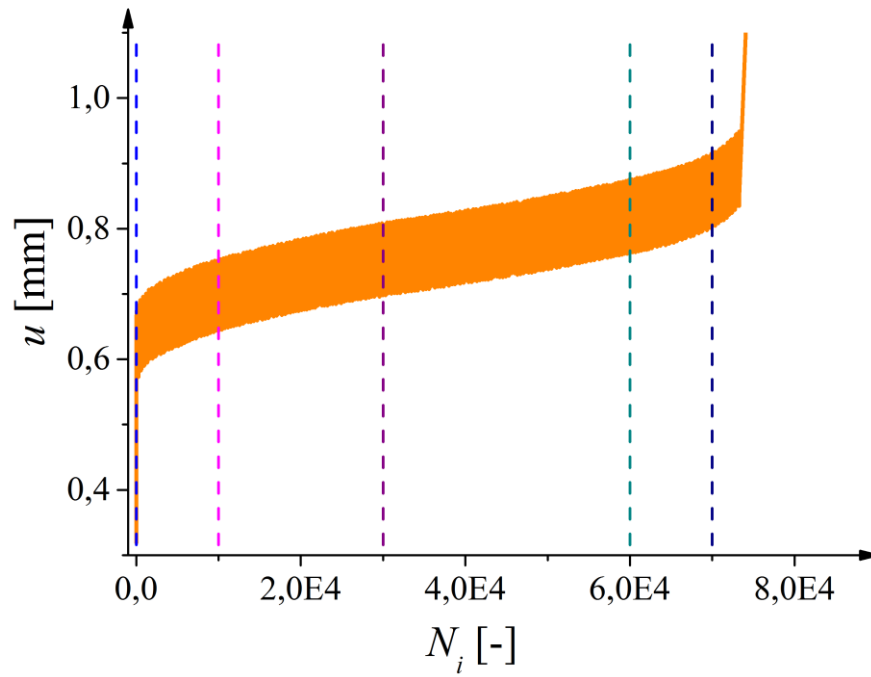


**Figure 6:** Experimental vertical normal stress  $\sigma$  versus vertical displacement  $u$  from monotonic and cyclic uniaxial compression tests (a) quasi-static test, b) fatigue test '1', c) fatigue test '2' and d) fatigue test '3')

**FIGURE 6**



605

606

607

608

609

610

611

612

613

614

615

616

617

618

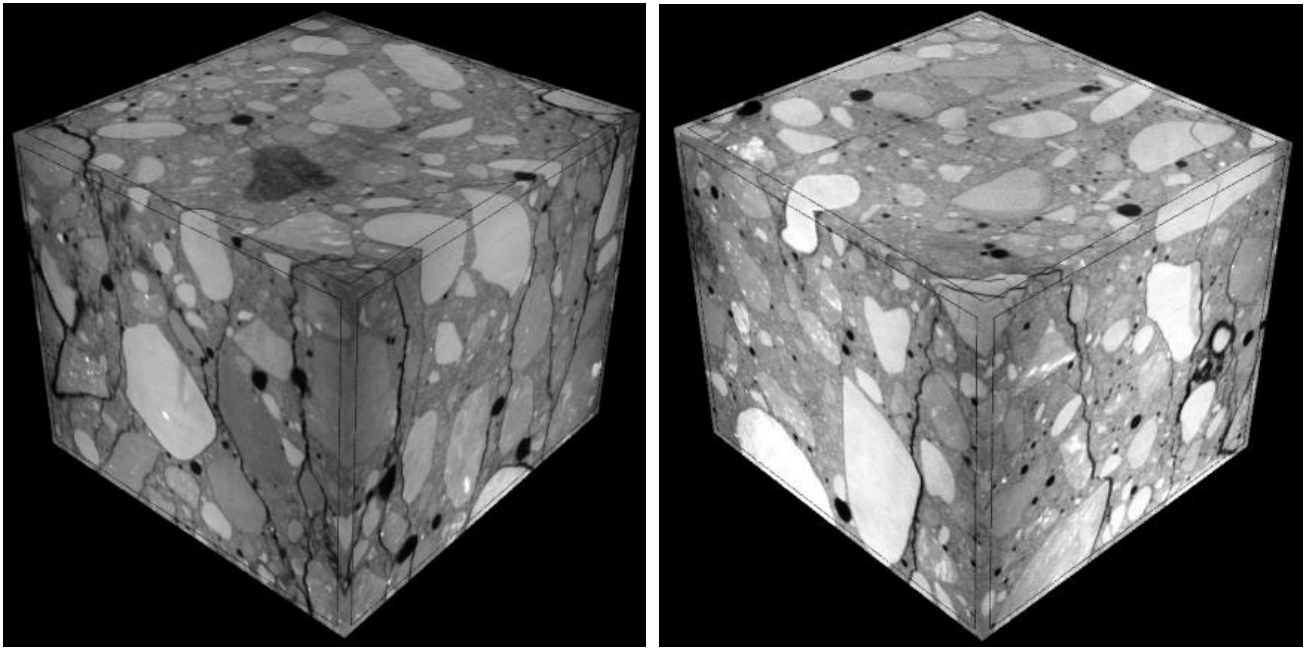
619

**Figure 7:** Experimental vertical displacement  $u$  from cyclic uniaxial compression tests versus the number of cycles  $N_i$  for concrete specimen '3' (vertical dashed lines denote breaks for X-ray micro-CT scanning)

**FIGURE 7**

619

620

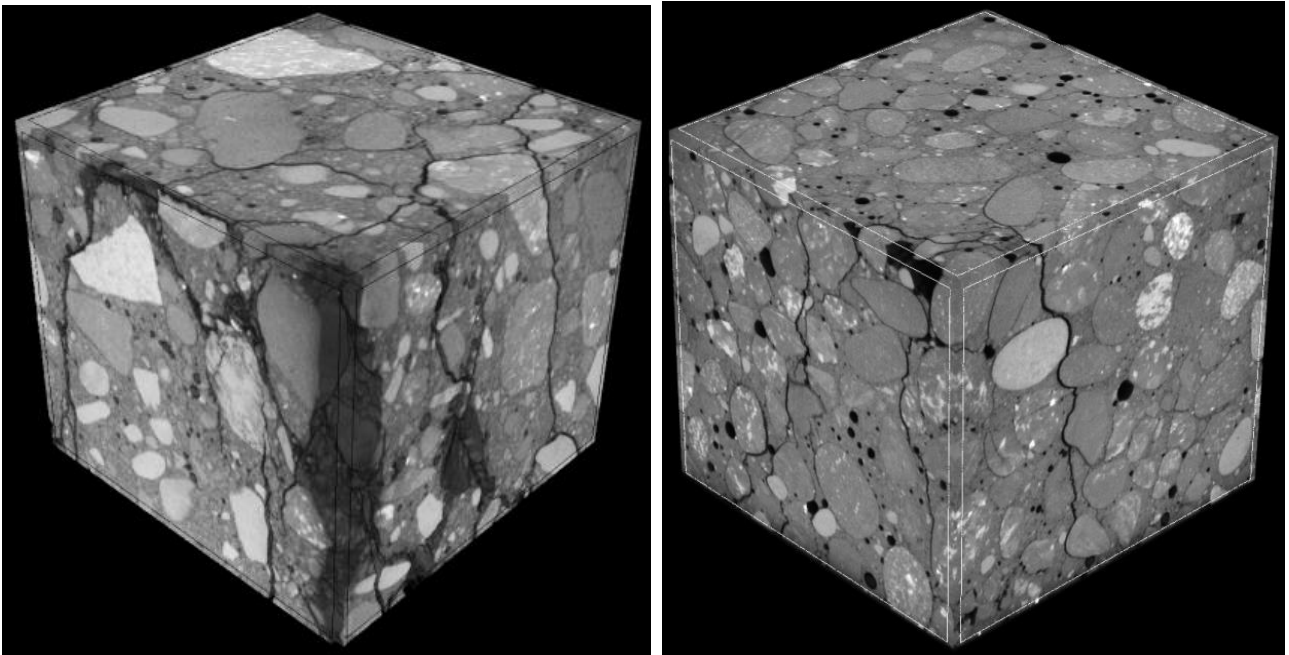


621

622

a)

b)



623

624

625

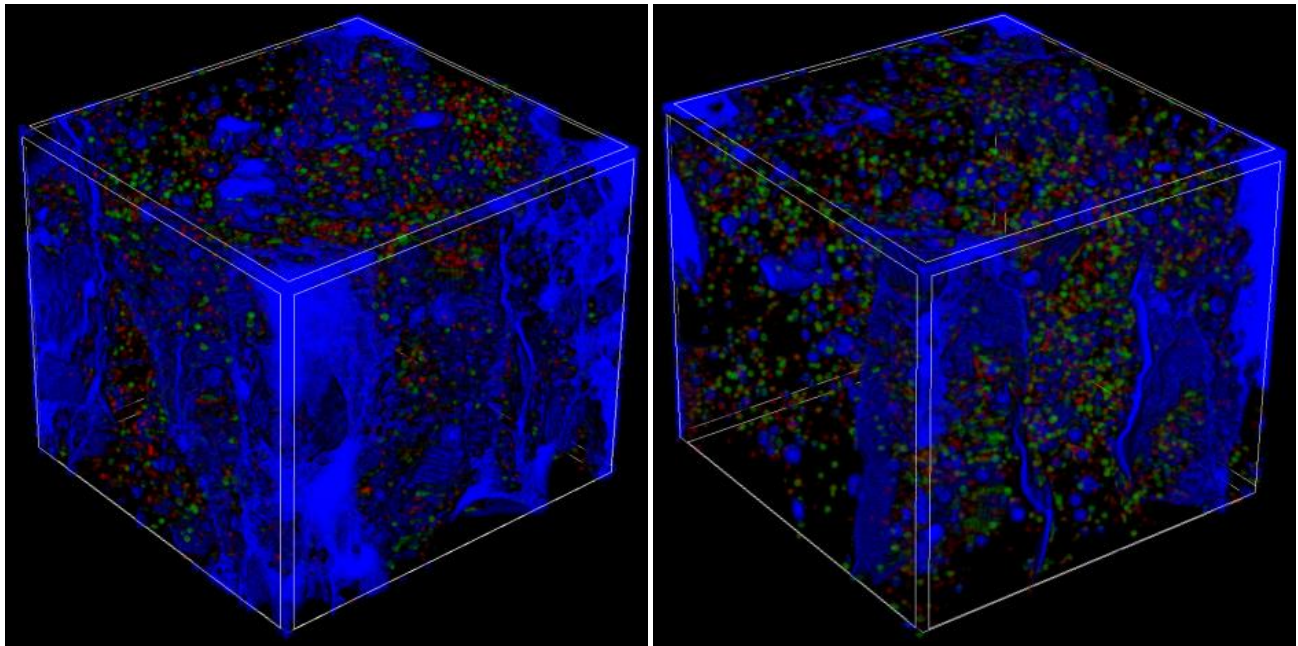
626

c)

d)

**Figure 8:** External 3D X-ray micro-CT images of cracked cubic concrete specimens close to failure during cyclic and monotonic tests in compression: a) specimen '1', b) specimen '2', c) specimen '3' in cyclic tests and d) specimen '0' in monotonic test (black colour denotes both pores and cracks)

**FIGURE 8**

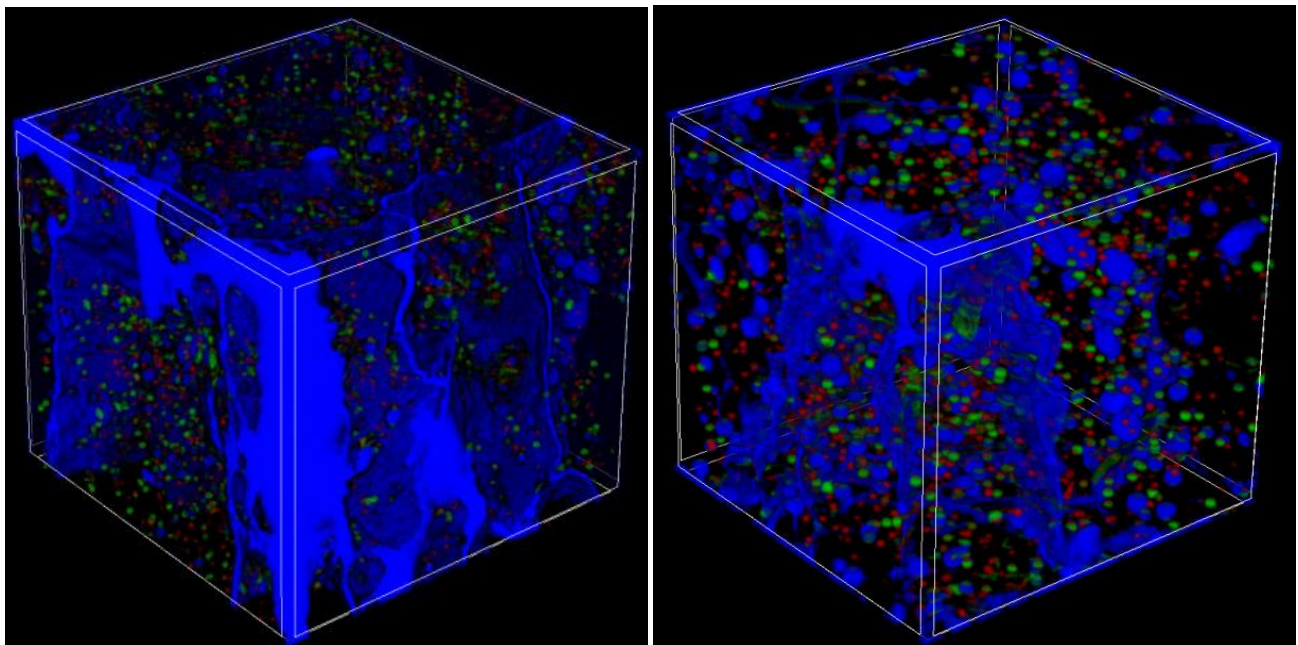


a)

b)

633

634



c)

d)

635

636

637

638

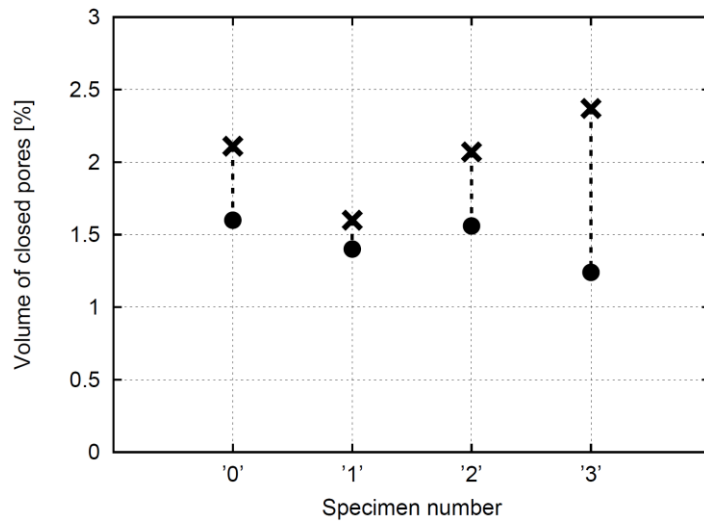
639

**Figure 9:** Internal 3D micro-CT images of pores and cracks in cubic concrete specimens close to failure during cyclic and monotonic tests: a) specimen '1' b) specimen '2', c) specimen '3' in cyclic tests and d) specimen '0' in monotonic test (colours denote macro-pores' diameter in range of  $\leq 1.0$  mm (red colour), 1.01 mm - 2.0 mm (green colour) and  $\geq 2.0$  mm (blue colour))

**FIGURE 9**

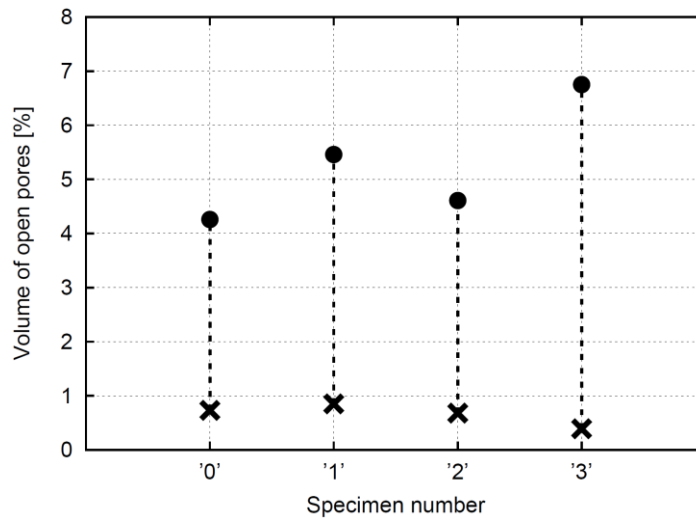
4





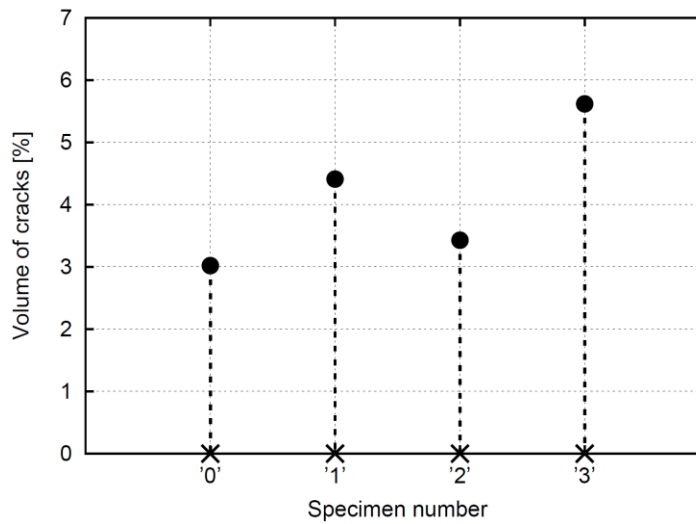
645

a)



646

b)



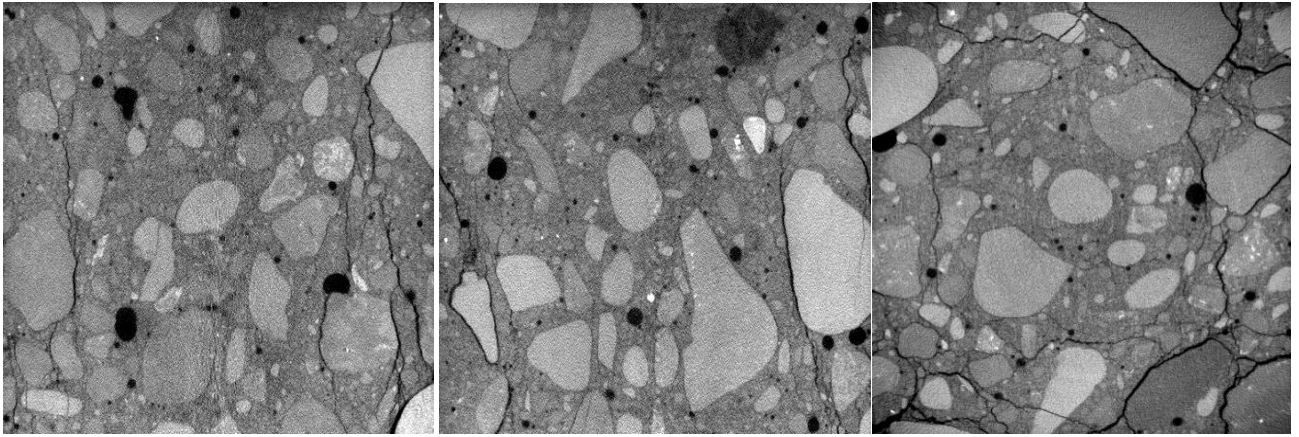
647

c)

**Figure 10:** Volume changes of pores and cracks in concrete specimens '0'-'3' during uniaxial fatigue compression: a) volume of closed pores, b) volume of open pores and c) volume of cracks (x - initial value before test and ● - final value after test)

**FIGURE 10**

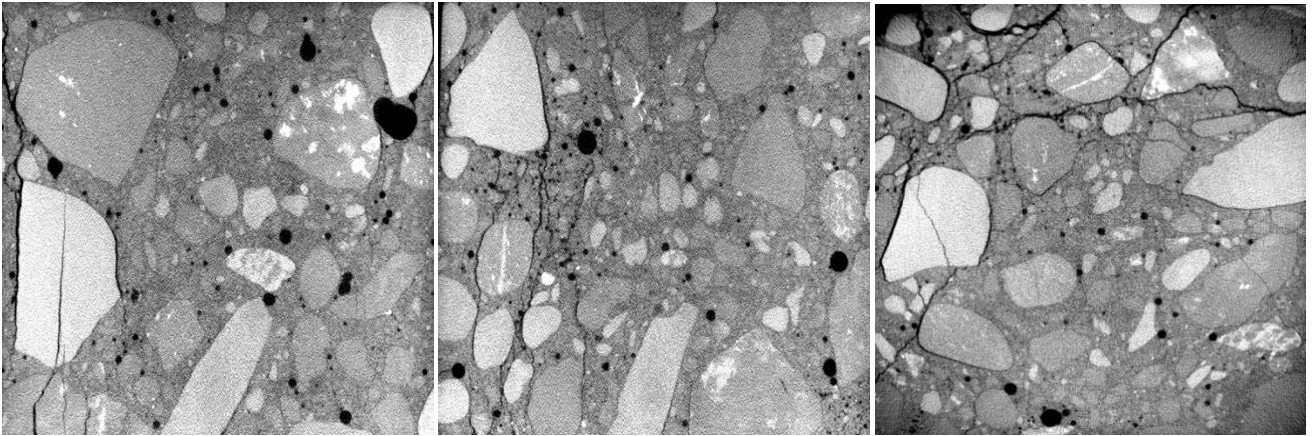
653



654

655

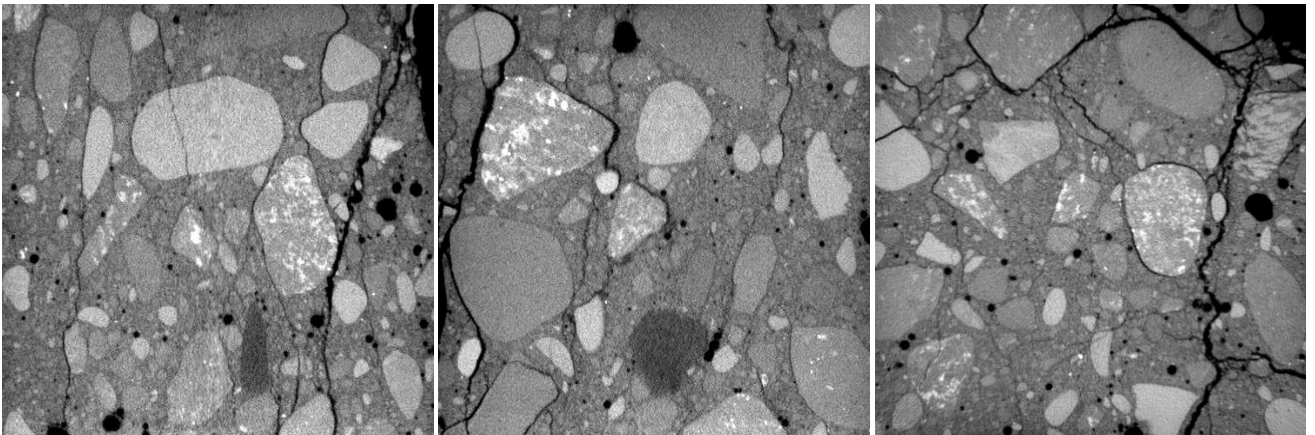
A)



656

657

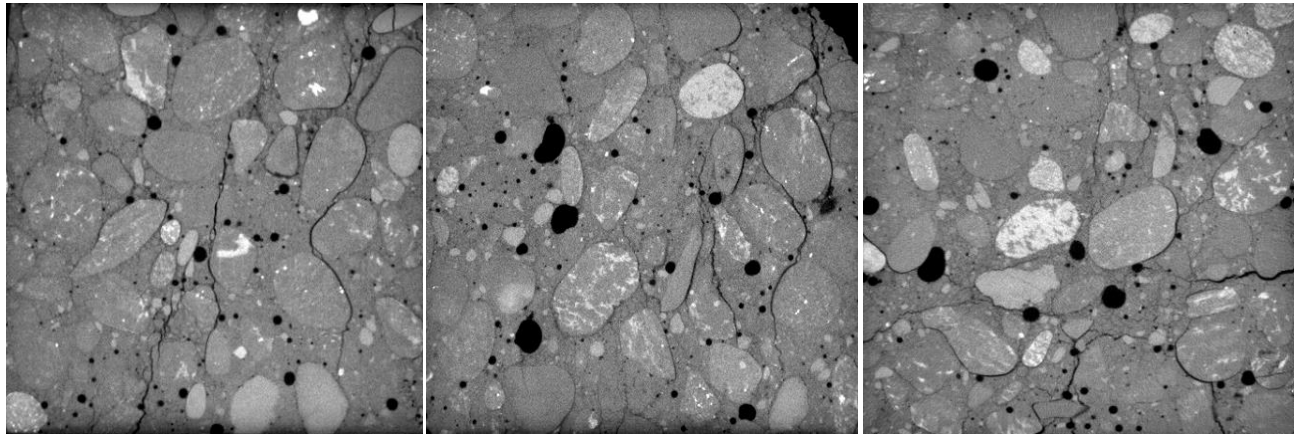
B)



658

659

C)



a)

D)

b)

c)

660

661

662

663

664

665

666

667

668

669

670

671

672

673

674

675

676

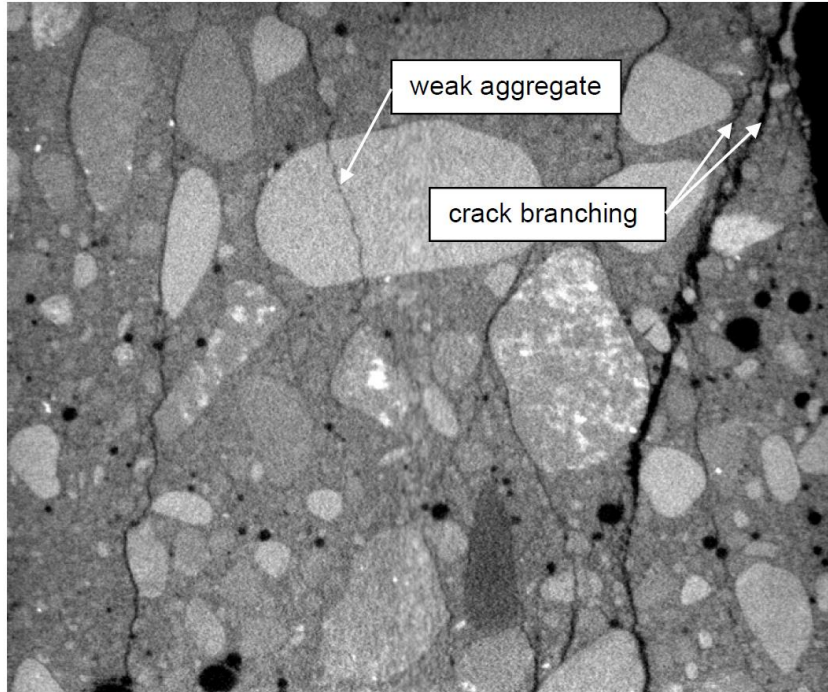
677

678

**Figure 11:** 2D micro-CT images of cracked cubic specimens close to failure: A) specimen '1', B) specimen '2', C) specimen '3' (fatigue tests) and D) specimen '0' (monotonic test) (a and b) two vertical mid-specimen cross-sections and c) horizontal mid-specimen cross-section, black colour denotes pores and cracks)

## FIGURE 11

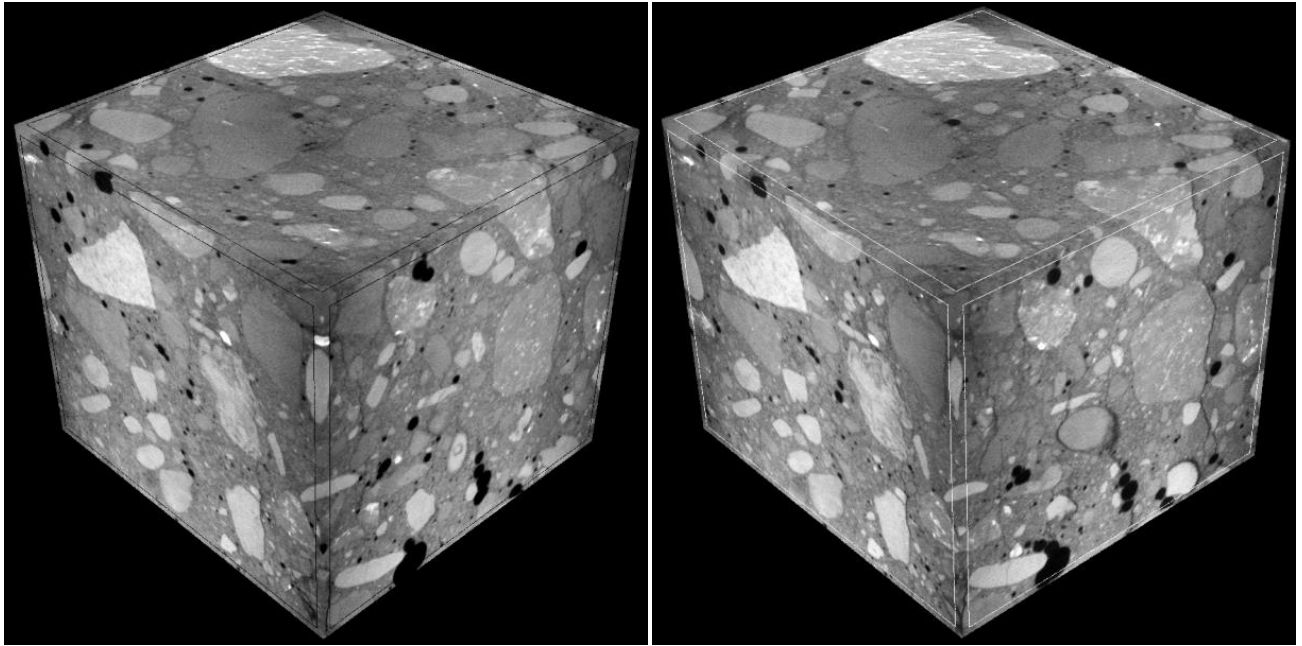
679  
680  
681  
682  
683



684  
685  
686  
687  
688  
689  
690  
691  
692

**Figure 12:** View on crack branching and crack propagating through weak aggregate particle

## FIGURE 12

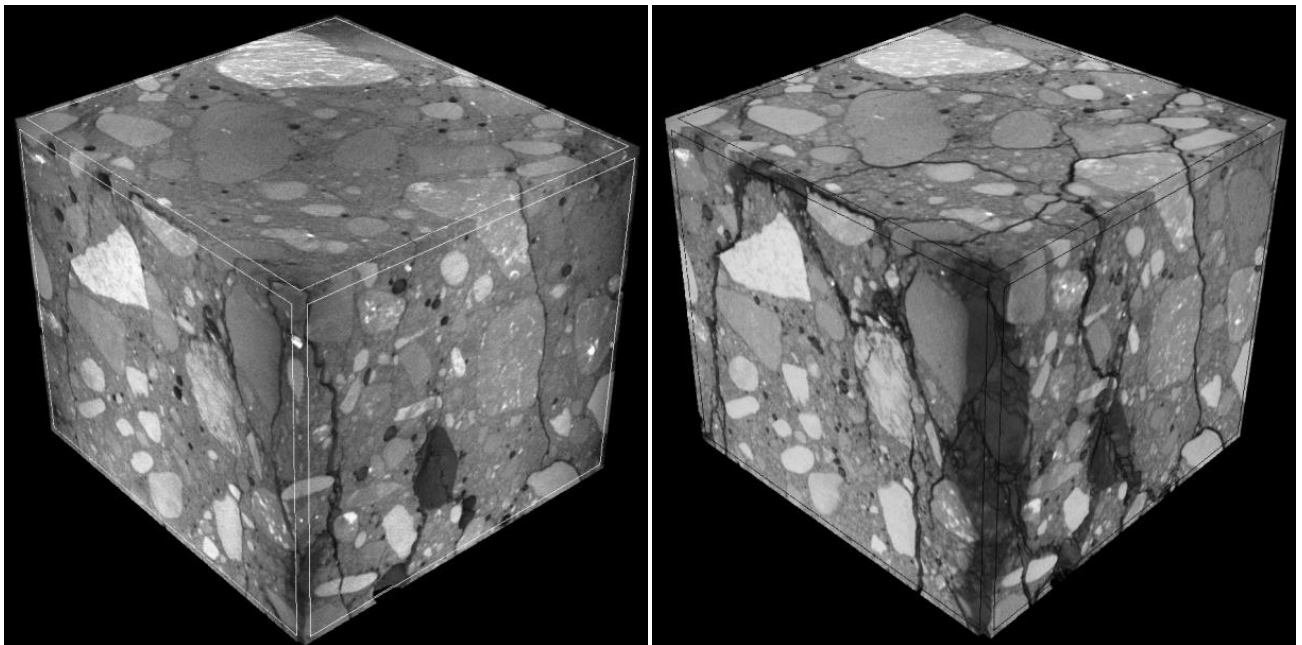


694

695

a)

b)



696

697

698

699

700

1

2

3

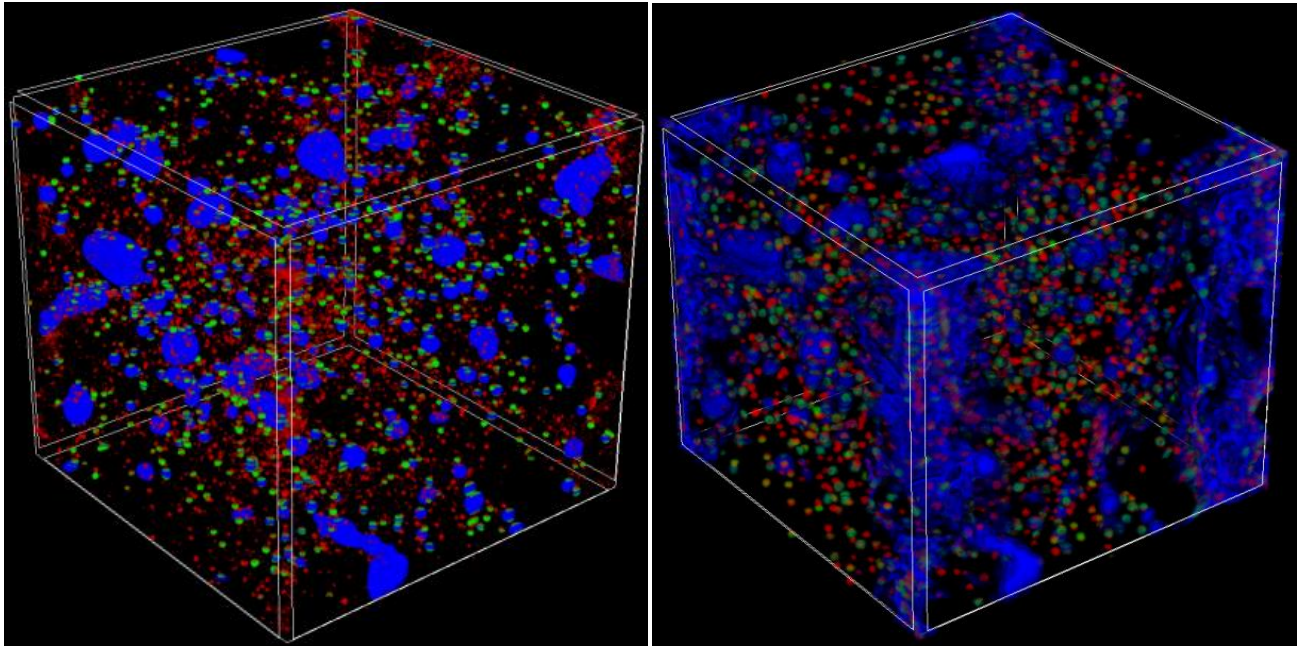
4

c)

d)

**Figure 13:** Cracking evolution in cubic concrete specimen '3' from 3D micro-CT images in fatigue tests: a) before test (Figure 4c), b) after  $N_3=30,000$  cycles c) after  $N_4=60,000$  cycles and d) after  $N_5=70,000$  cycles

**FIGURE 13**

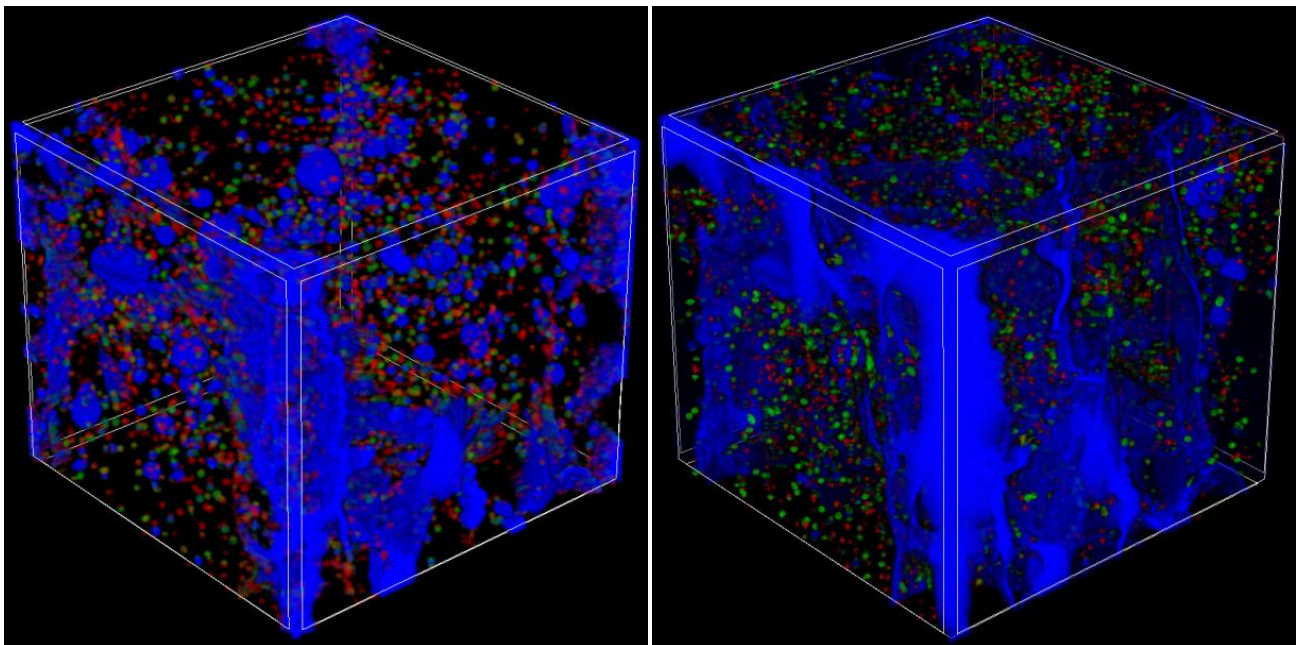


706

707

a)

b)



708

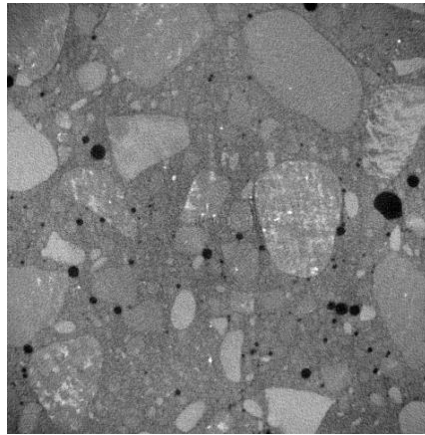
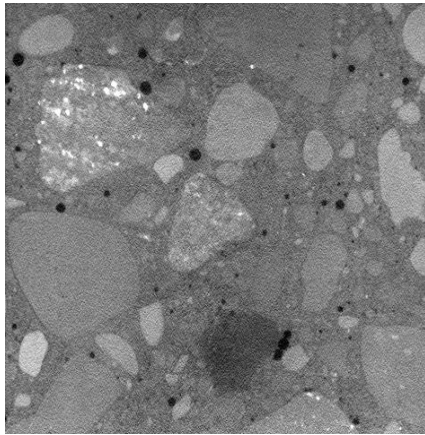
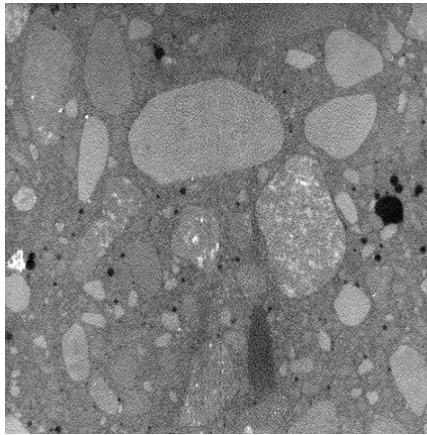
709

c)

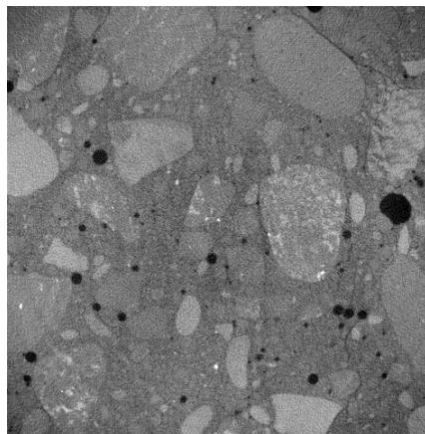
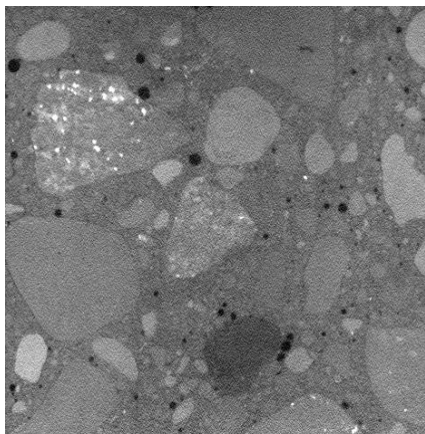
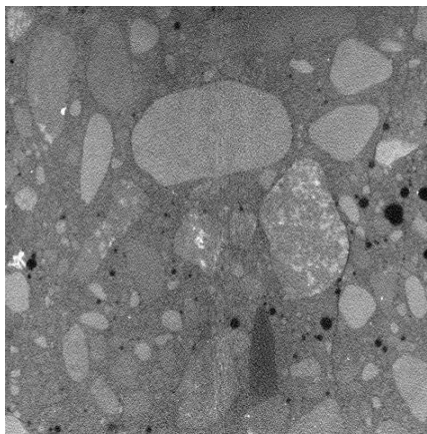
d)

**Figure 14:** Evolution of pores and cracks in cubic concrete specimen '3' from 3D micro-CT images in fatigue tests: a) before test (Figure 5c), b) after 30,000 loading cycles c) after 60,000 loading cycles and d) after 70,000 loading cycles (colours denote pores' diameter in range of  $\leq 1.0$  mm (red colour), 1.01 mm - 2.0 mm (green colour) and  $\geq 2.0$  mm (blue colour))

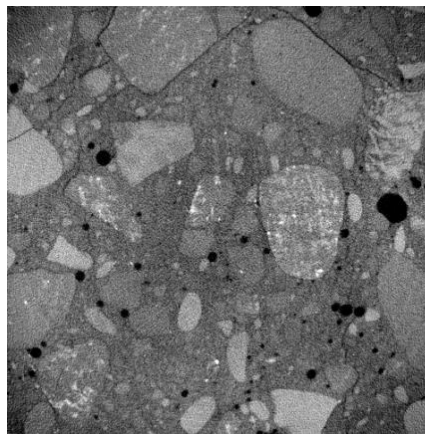
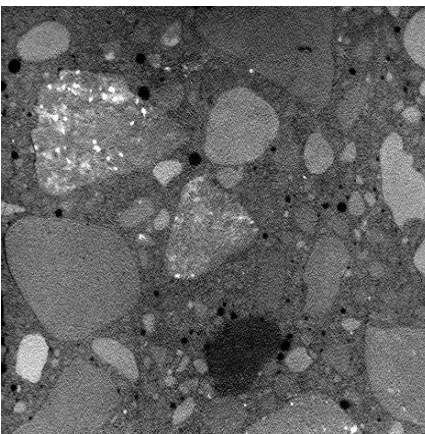
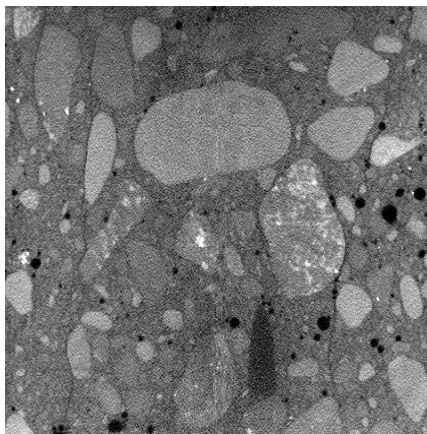
**FIGURE 14**



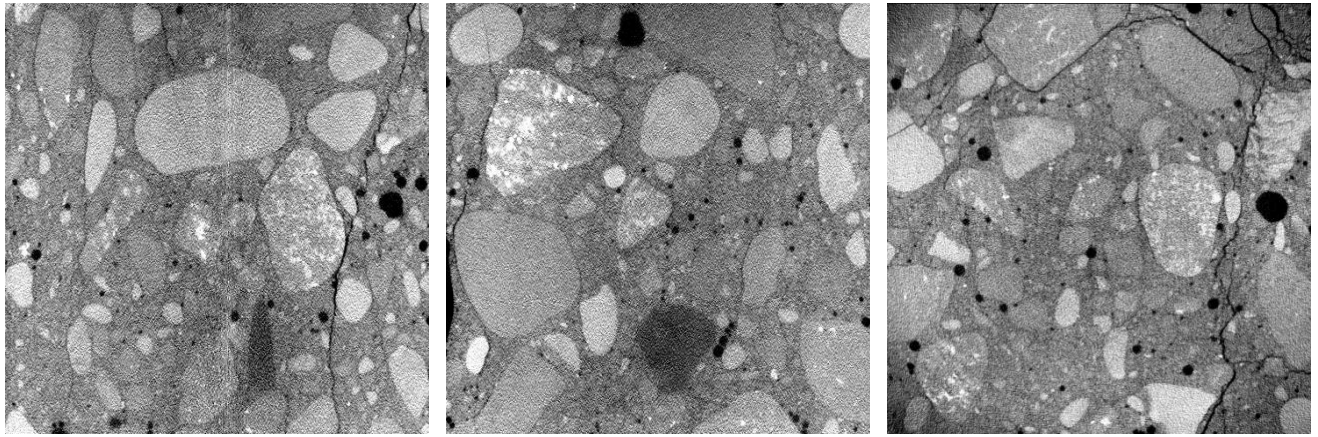
A)



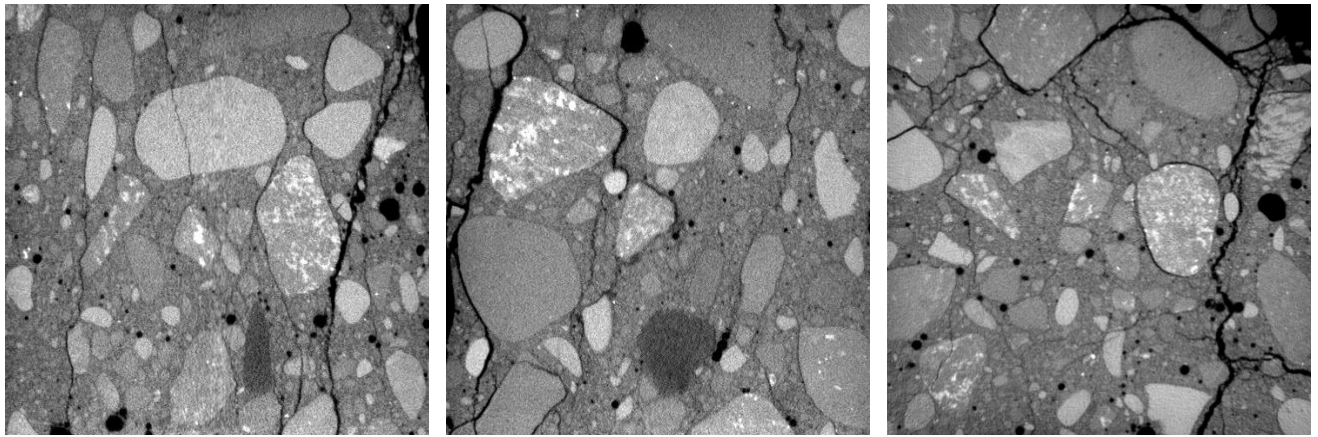
B)



C)



D)



E)

a)

b)

c)

717

718

719 **Figure 15:** 2D micro-CT images of cracked cubic specimen '3' for different deformation steps:

720 A) step "0", B) step 1", C) step "2", D) step "3" and E) step "4" (a) and b) two vertical mid-specimen

721 cross-sections and c) horizontal mid-specimen cross-section, black colour denotes pores and macro-

722 cracks)

723

724

725

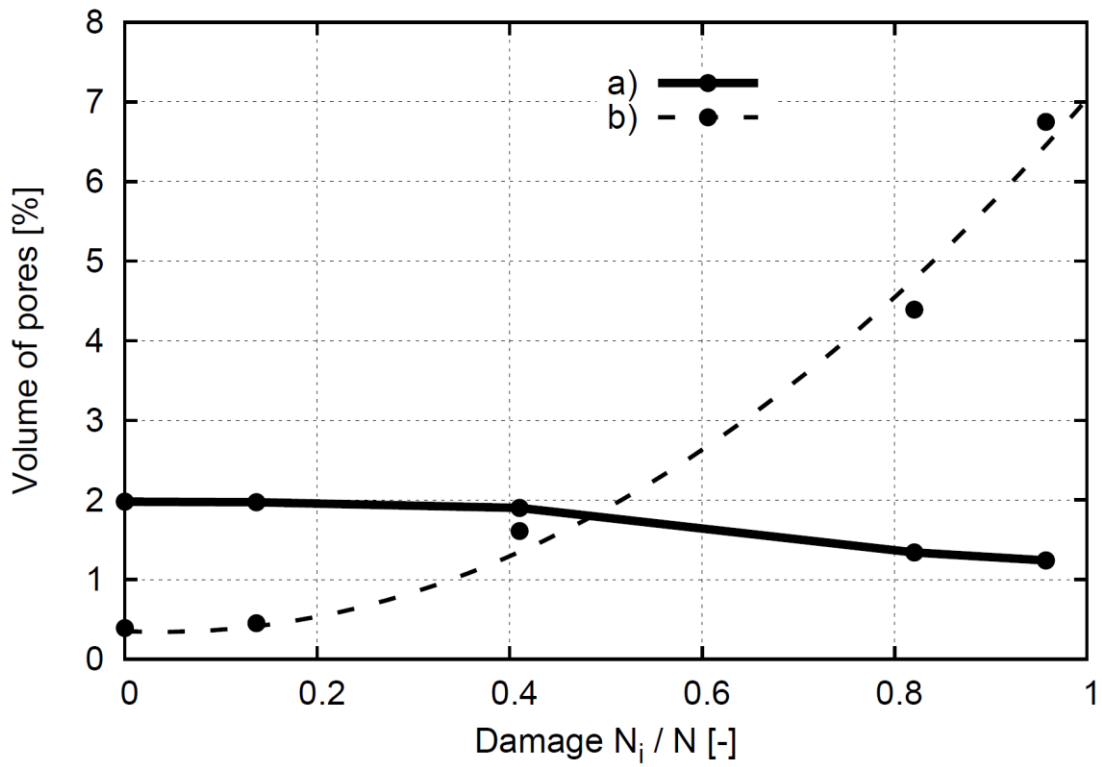
726

727

**FIGURE 15**



728  
729  
730



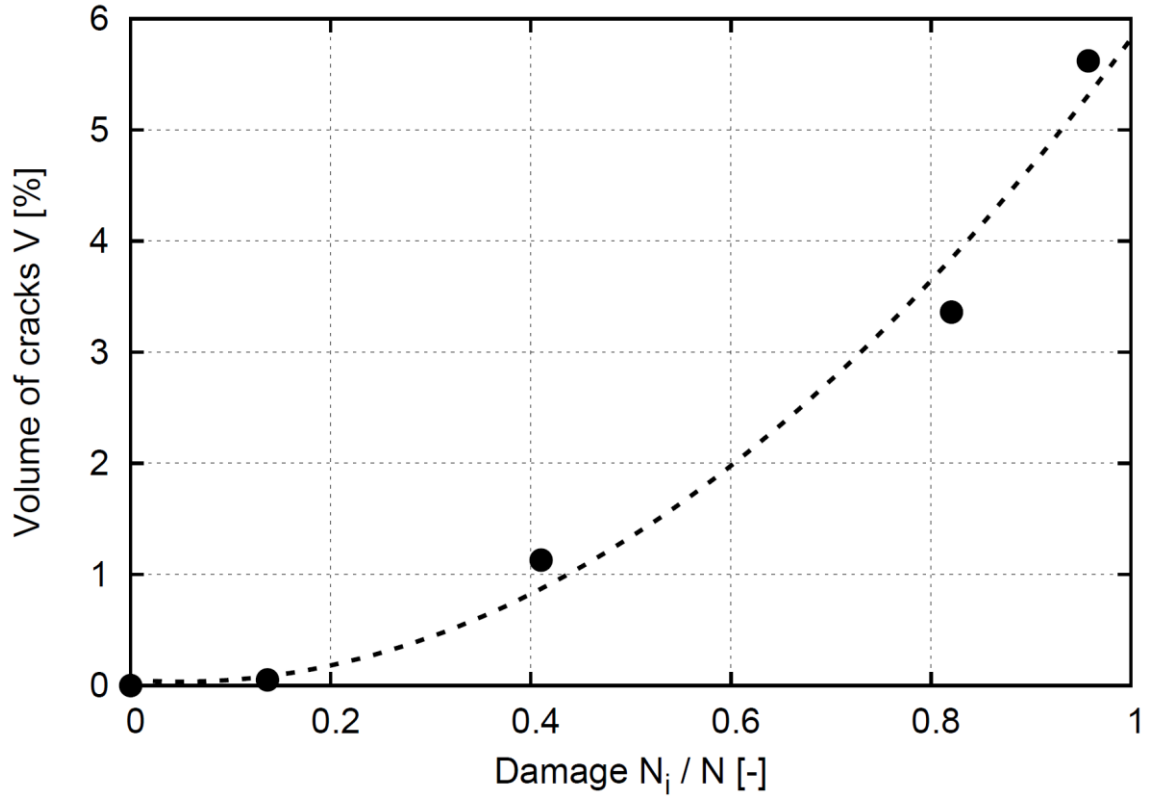
731  
732  
733  
734  
735  
736

**Figure 16:** Evolution of volume of closed pores (a) and open pores (b) with increasing damage (expressed by quotient of number of loading cycles  $N_i$  and fatigue life  $N$ ) in concrete specimen '3'

**FIGURE 16**

737  
738  
739

740  
741  
742  
743  
744  
745



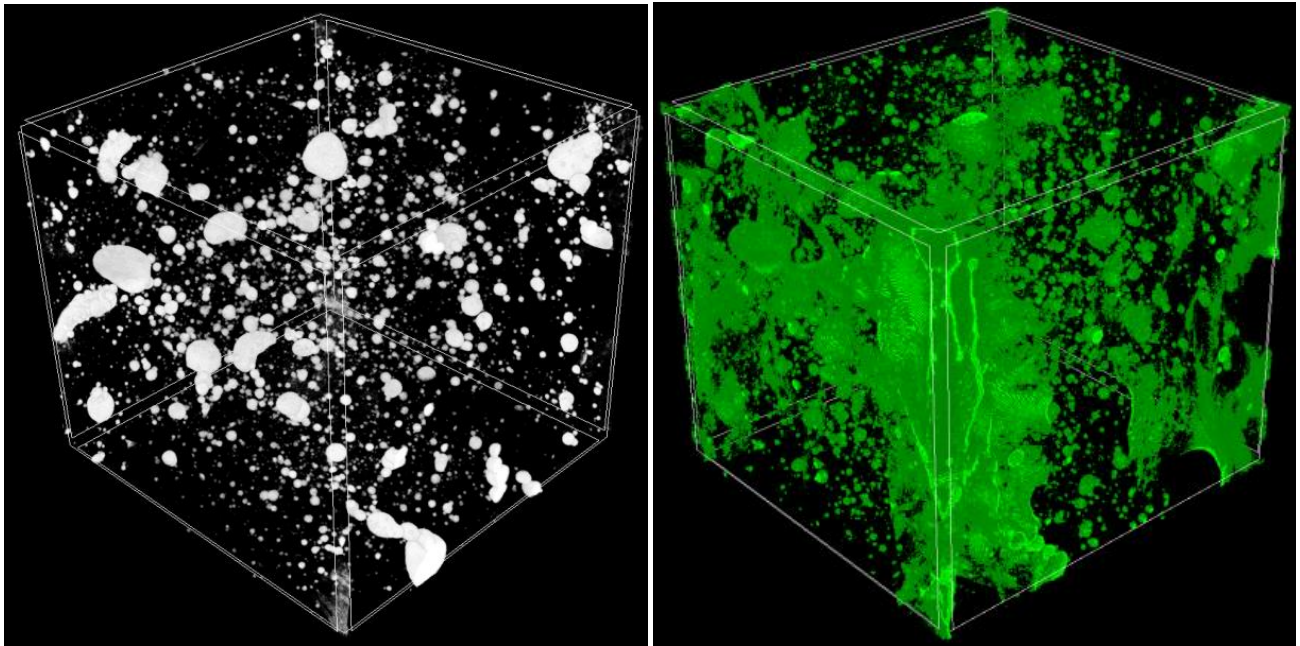
746  
747  
748  
749

**Figure 17:** Evolution of crack volume  $V$  versus damage (expressed by quotient of number of loading cycles  $N_i$  and fatigue life  $N$ ) in concrete specimen '3'

750  
751  
752  
753  
754  
755

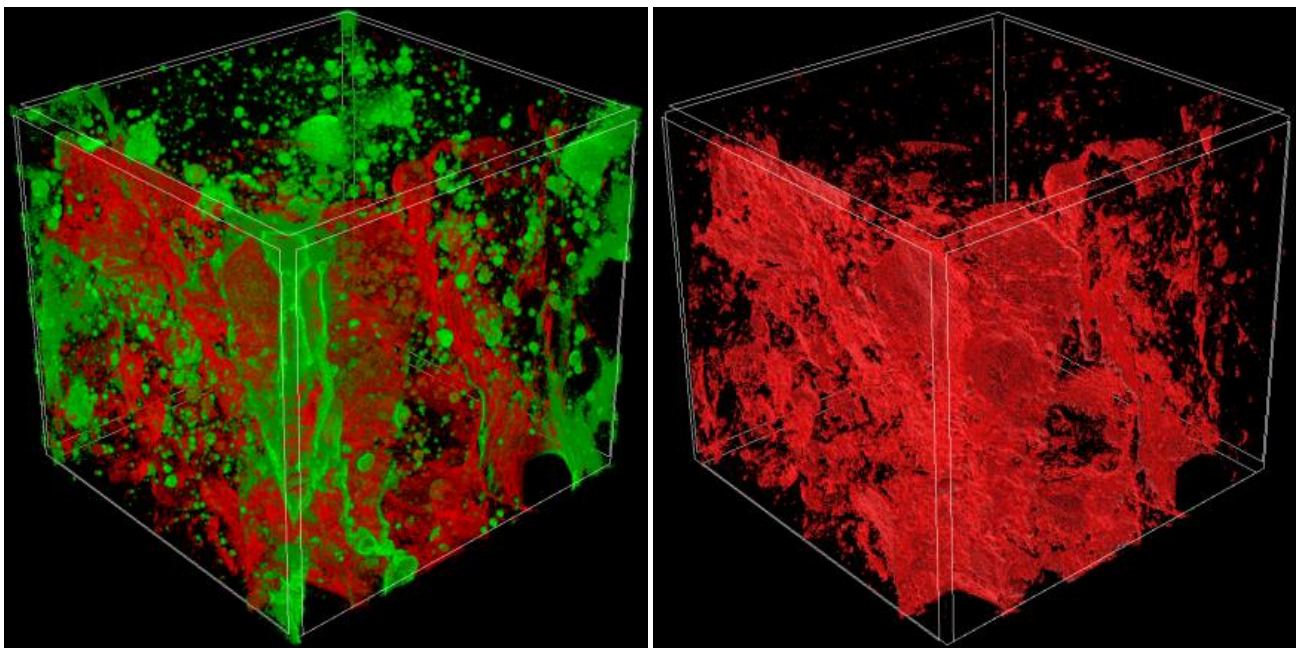
**FIGURE 17**

6  
7  
8



a)

b)



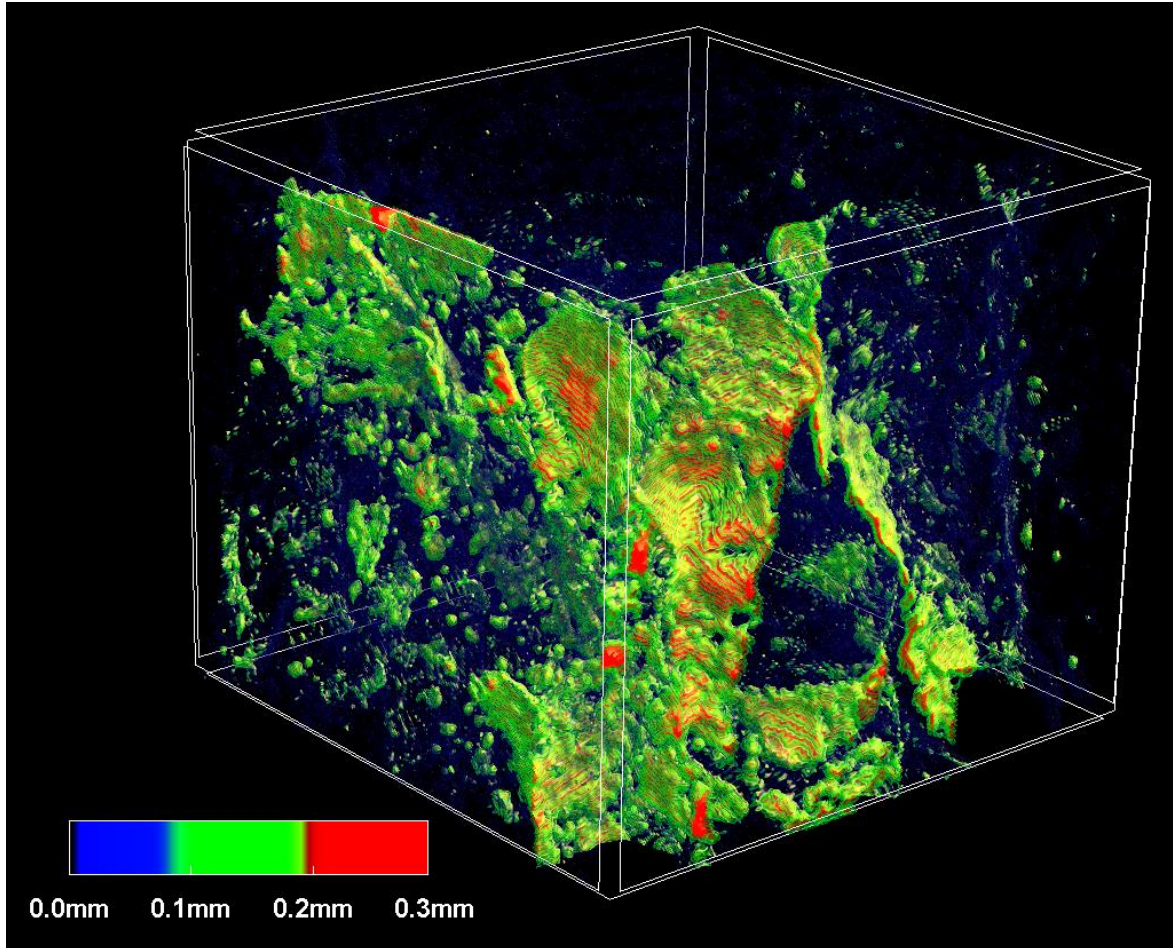
c)

d)

**Figure 18:** Distribution of pores and cracks in specimen '3': a) non-cracked concrete specimen (white colour), b) after  $N_4=60,000$  cycles (green colour), c) after  $N_5=70,000$  loading cycles (green and red colour) and d) between  $N_4=60,000$  and  $N_5=70,000$  cycles (red colour)

**FIGURE 18**

771  
772  
773  
774  
775



776

777  
778  
779  
780  
781  
782  
783  
784  
785  
786  
787  
788  
789  
790  
791  
792  
793  
794  
795  
796  
797  
798  
799  
800  
801  
802  
803  
804  
805  
806  
807  
808  
809  
810  
811  
812  
813  
814  
815  
816  
817  
818  
819  
820  
821  
822  
823  
824  
825  
826  
827  
828  
829  
830  
831  
832  
833  
834  
835  
836  
837  
838  
839  
840  
841  
842  
843  
844  
845  
846  
847  
848  
849  
850  
851  
852  
853  
854  
855  
856  
857  
858  
859  
860  
861  
862  
863  
864  
865  
866  
867  
868  
869  
870  
871  
872  
873  
874  
875  
876  
877  
878  
879  
880  
881  
882  
883  
884  
885  
886  
887  
888  
889  
890  
891  
892  
893  
894  
895  
896  
897  
898  
899  
900  
901  
902  
903  
904  
905  
906  
907  
908  
909  
910  
911  
912  
913  
914  
915  
916  
917  
918  
919  
920  
921  
922  
923  
924  
925  
926  
927  
928  
929  
930  
931  
932  
933  
934  
935  
936  
937  
938  
939  
940  
941  
942  
943  
944  
945  
946  
947  
948  
949  
950  
951  
952  
953  
954  
955  
956  
957  
958  
959  
960  
961  
962  
963  
964  
965  
966  
967  
968  
969  
970  
971  
972  
973  
974  
975  
976  
977  
978  
979  
980  
981  
982  
983  
984  
985  
986  
987  
988  
989  
990  
991  
992  
993  
994  
995  
996  
997  
998  
999  
1000

**Figure 19:** Micro-CT image of distribution of crack width's growth between  $N_4=60,000$  and  $N_5=70,000$  cycles in concrete specimen '3' of Figure 18d

**FIGURE 19**

790  
791  
792  
793  
794  
795  
796

## LIST OF TABLES

**Table 1:** Concrete mixing composition in experiments ( $d_{50}$  – mean particle diameter,  $d_{max}$  – maximum particle diameter and  $\beta$  – total particle volume)

<b>Concrete component</b>	<b>Content of concrete components</b> ( $d_{50}=2$ mm, $d_{max}=16$ mm, $\beta=75\%$ )
cement (Portland 32.5R)	810 [kg/m <sup>3</sup> ]
sand (diameter size 0-2 mm)	650 [kg/m <sup>3</sup> ]
gravel (diameter size 2-8 mm)	580 [kg/m <sup>3</sup> ]
gravel (diameter size 8-16 mm)	580 [kg/m <sup>3</sup> ]
water	340 [l/m <sup>3</sup> ]

797  
798  
799

800

801 **Table 2:** Volume and diameter range of macro-pores in initial non-cracked concrete specimens

802 (specimens '1'-'3' are presented in Figure 4)

803

Specimen number and test type	Diameter range of pores [%]				Volume of pores [mm <sup>3</sup> ]	% - volume of pores [%]	% - volume of closed pores [%]	% - volume of open pores [%]
	≤0.50 mm	0.51-1.00 mm	1.01-2.00 mm	≥2.01 mm				
'0' monotonic test	12.2	11.9	28.5	47.4	1817.6	2.84	2.11	0.73
'1' fatigue test	10.2	15.4	30.5	43.9	1568.4	2.45	1.60	0.85
'2' fatigue test	14.5	16.4	22.2	46.9	1760.2	2.75	2.07	0.68
'3' fatigue test	9.8	14.1	24.5	51.6	1516.8	2.37	1.98	0.39

804

805

806

807 **Table 3:** Fatigue life results (maximum number of loading cycles leading to specimen failure) for808 concrete specimens '1'-'3' during uniaxial compression ( $\sigma_{max}$  - maximum normal stress,  $\sigma_{min}$  - minimum809 normal stress and  $f_c$  - uniaxial compressive strength)

810

Concrete specimen	$\sigma_{max}/f_c$	$\sigma_{min}/f_c$	Number of fatigue life cycles
'1'	0.75	0.37	71,518
'2'			80,069
'3'			73,127

1

2

813 **Table 4:** Volume of pores and cracks in concrete specimens ‘1’-‘3’ after 70,000 cycles and in concrete  
 814 specimen ‘0’ after monotonic loading close to failure  
 815

Specimen number and test type	Volume of pores and cracks [mm <sup>3</sup> ]	% - volume of pores and cracks [%]	% - volume of closed pores and cracks [%]	% - volume of open pores and cracks [%]	Volume of cracks [mm <sup>3</sup> ]	% - volume of cracks [%]
‘0’ monotonic test	3750.4	5.86	1.60	4.26	1932.8	3.02
‘1’ fatigue test	4390.4	6.86	1.40	5.46	2822.0	4.41
‘2’ fatigue test	3948.8	6.17	1.56	4.61	2188.6	3.43
‘3’ fatigue test	5113.6	7.99	1.24	6.75	3596.8	5.62

816  
 817  
 818  
 819  
 820  
 821

**Table 5:** Volume of pores and cracks in concrete specimen ‘3’ for different steps related to numbers of cycles  $N_i$

Step	Number of cycles $N_i$	Volume of pores and cracks [mm <sup>3</sup> ]	% - volume of pores and cracks [%]	% - volume of closed pores and cracks [%]	% - volume of open pores [%]	Volume of cracks [mm <sup>3</sup> ]	% - volume of cracks [%]
‘1’	0	1516.8	2.37	1.98	0.39	0	0
‘2’	10,000	1548.8	2.42	1.97	0.45	32.0	0.05
‘3’	30,000	2240.0	3.50	1.90	1.61	723.2	1.13
‘4’	60,000	3667.2	5.73	1.34	4.39	2150.4	3.36
‘5’	70,000	5113.6	7.99	1.24	6.75	3596.8	5.62

2  
 3